Electro-driven self-assembly of valence-regulation interphase unlocks high energy and power densities in zinc-ion batteries

Yi-Chun Yang, Wei-Lun Sung, Chi-Wei Chou, Hung-Yang Yeh, Hsing-Yu Tuan

PII: S1385-8947(25)13370-6

DOI: https://doi.org/10.1016/j.cej.2025.172521

Reference: CEJ 172521

To appear in:

Received date: 23 October 2025

Revised date: 28 December 2025

Accepted date: 30 December 2025

Please cite this article as: Y.-C. Yang, W.-L. Sung, C.-W. Chou, et al., Electro-driven self-assembly of valence-regulation interphase unlocks high energy and power densities in zinc-ion batteries, (2024), https://doi.org/10.1016/j.cej.2025.172521

Electro–Driven Self–Assembly of Valence–Regulation Interphase Unlocks High Energy and Power Densities in Zinc–Ion Batteries

Yi–Chun Yang [a,1], *Wei–Lun Sung* [a,1], *Chi–Wei Chou* [a], *Hung–Yang Yeh* [a], *and Hsing–Yu Tuan* [a,b,*]

[a] Department of Chemical Engineering, National Tsing Hua University, Hsinchu, 30013, Taiwan

[b] Department of Chemical Engineering, Chung Yuan Christian University, Chungli, Taoyuan, 32023, Taiwan

*Corresponding Authors:

Email: hytuan@che.nthu.edu.tw

Phone: (886)3–571–5131 ext. 42509

[1]Y.–C. Y. and W.–L. S. equally contributed to this work.

Abstract

The development of safe, sustainable, and high–rate grid–scale energy storage has intensified interest in aqueous zinc–ion batteries (AZIBs), yet cathode–electrolyte interfacial instability remains a bottleneck. Here, we present a controllable electro–driven self–assembly strategy to construct adaptive, valence–regulating interphases on VO_2 cathodes. Electrochemical activation induces VO^{2+}–H_2O coordination, forming compact interphases enriched in high–valence V^{5+}. Modulating activation kinetics–higher rates (0.5 A g^{-1}) producing denser, more stable layers than lower rates (0.1 A g^{-1})–precisely controls growth uniformity, optimizes ion transport, and stabilizes interfacial redox processes. These interphases homogenize electric fields, suppress vanadium dissolution, and expose abundant active sites, sustaining long–term structural integrity. Simultaneously, VO_2 undergoes in situ reconstruction into $V_2O_5{\cdot}nH_2O$, enabling reversible multielectron V^{4+}/V^{5+} transitions and accelerating Zn^{2+} diffusion. This kinetics–governed assembly achieves high capacity and remarkable rate capability (20 A g^{-1}), and pouch cells deliver competitive energy (842.8 W h kg^{-1}) and power densities in AZIBs. This work establishes a unified interphase engineering strategy that integrates self–assembly with valence modulation, offering a broadly applicable platform for interfacial regulation in aqueous energy storage systems.

Keywords: self–assembled; electro–derived; zinc ion batteries; valence–regulation; interphase

1. Introduction

Amid the accelerating global pursuit of carbon neutrality, the demand for large–scale, reliable, and economically viable energy storage technologies has grown substantially.[1-5] While solar and wind power offer significant environmental benefits, their inherent intermittency and variability challenge grid reliability, making electrochemical energy storage systems indispensable for ensuring energy security and stability. With high reversible capacity, natural abundance, and environmental safety, aqueous zinc–ion batteries (AZIBs) have emerged as promising candidates for cost–effective and sustainable energy storage.[6-12] Nevertheless, their practical deployment is hindered by persistent interfacial challenges, particularly the instability of the cathode–electrolyte interface. In vanadium–based cathodes (e.g., VO, V_2O_3, VO_2, V_2O_5), multiple accessible oxidation states (+2 to +5) enable rich redox chemistry but also render the crystal structure susceptible to degradation. Zn^{2+} insertion shifts V–O bonds toward lower binding energies due to competition between Zn–O and V–O interactions, while the high charge density of Zn^{2+} imposes strong electrostatic attraction to the host lattice.[13, 14] Combined with anion–cation interactions and cation polarization, these effects slow ion diffusion during faradaic processes. At the electrode–electrolyte interface, side reactions yield inert byproducts such as basic zinc salts ($Zn_4SO_4(OH)_6{\cdot}nH_2O$) and vanadium–containing phases ($Zn_3(OH)_2V_2O_7{\cdot}2H_2O$), which block active Zn^{2+} adsorption sites and hinder ion transport.[15] Vanadium dissolution, further accelerated under acidic conditions via proton–vanadium interactions, depletes active material and destabilizes the host

framework. Moreover, $H_2O/H^+/Zn^{2+}$ co–insertion–while beneficial for structural flexibility, interlayer expansion, and Zn^{2+} screening–also exacerbates byproduct accumulation, whose poor reversibility undermines long–term cycling stability.[16, 17]

Interphase design has emerged as a central strategy for advancing AZIBs, as interphases critically govern ion transport, redox kinetics, and long–term cycling stability.[18, 19] While cathodic interphases play a decisive role in regulating redox processes and structural evolution, research on interphase engineering in AZIBs has been overwhelmingly directed toward the zinc anode.[20] At the anode side, numerous strategies–primarily functional electrolyte additives and surface modifications–have been developed to stabilize interfaces, suppress dendrite growth, and mitigate parasitic reactions.[21] For example, π–conjugated quinone polymers (PPPA) and hydrolyzed polymaleic anhydride (HPMA) can coordinate with Zn^{2+} to facilitate desolvation and guide uniform deposition, while in–situ decomposition strategies such as $ZnSiF_6$–derived ZnF_2 improve Zn^{2+} utilization and extend cycling life.[22, 23] More recently, functional additives have been designed to induce in–situ SEI–like interphases for enhanced anode stability; [24, 25] for instance, difluoromethyl oxalate (DFMO), a fluorinated additive that decomposes to form a stabilizing interphase, generates a ZnF_2–rich layer via electrochemical reactions. Likewise, silane–based coupling agents can form gel–like interphases through hydrolysis. Both strategies significantly improve corrosion resistance and Zn^{2+} transport.[26] These advances highlight the effectiveness of anode–side interphase engineering in improving reversibility and rate capability. Nevertheless, such

strategies remain constrained by intrinsic drawbacks, including interfacial fragility, poor adhesion, and insufficient ionic conductivity at high current densities, which often lead to interphase breakdown, dendritic proliferation, and passivation. More importantly, the cathodic interface–despite undergoing substantial electrochemical reconstruction and strongly influencing redox kinetics–has received far less attention. The rational design of in–situ generated cathodic interphases therefore represents a crucial yet underexplored pathway, requiring innovative concepts to couple interfacial stability with redox functionality.

Beyond conventional interphase design, self–assembly strategies have emerged as powerful tools to construct ordered and functional protective architectures in electrochemical systems.[27, 28] By harnessing the spontaneous aggregation of molecules or nanosheets, self–assembled layers can conformally cover electrode surfaces, regulate ion flux, and suppress degradation. For example, aminopropylphosphonic acid molecules assemble on MnO_2 to form a ~6 nm protective film that inhibits Mn^{2+} dissolution; protein–derived microsphere coatings redistribute ionic flux on Li metal to mitigate dendrites;[29] few–layer MXene nanosheets assemble on VS_2 to build conductive 2D frameworks that enhance charge transfer;[30] and pyridine derivatives in Zn electrolytes form ZnI_2–enriched SEIs that suppress corrosion and hydrogen evolution.[31] While self–assembly enhances structural ordering and interfacial robustness, achieving optimal electrochemical performance also requires fine–tuning the intrinsic electronic structure of active materials–an aspect addressed by valence regulation. Valence regulation has been widely applied to optimize electronic structures, interfacial charge transfer, and redox reversibility in electrodes, and is increasingly recognized as an effective interphase engineering strategy. Incorporating polyoxometalates into HAVO promotes electron

delocalization by tuning V valence states;[32] F^- and Zn^{2+} co–coordination stabilizes Mn–based cathodes by mitigating Jahn–Teller distortion;[33] valence adjustment in NiCoMg–LDHs improves orbital overlap and ion adsorption;[34] and heteroatom modification in Li–based cathodes induces Mn^{3+} generation and oxygen vacancies to enhance diffusion and durability.[35] These studies reveal that interfacial self–assembly enables structural ordering and stability, while valence regulation directly governs electron density, redox efficiency, and ion transport dynamics. Integrating these complementary approaches into cathodic interphase design for AZIBs therefore offers a promising pathway to construct adaptive interphases capable of simultaneously regulating Zn^{2+} flux and transition–metal valence states, thereby unlocking high energy and power performance.

In this study, an electro–derived self–assembly approach is developed to construct the valence–regulating interphases enriched with high–valence V^{5+} species on VO_2 cathodes. As illustrated in **scheme 1**, these interphases spontaneously form at the cathode surface during the initial electrochemical activation through a self–assembly process involving electrolyte–derived VO^{2+} ions and H_2O molecules. The formation of uniform and compact interphases can be precisely regulated by adjusting the activation current density. A higher current density (0.5 A g^{-1}) promotes the growth of dense and homogeneous interphases, thereby enhancing local redox kinetics and accelerating nucleation and growth. In contrast, lower current densities induce sparse and irregular interphases, leading to less effective interfacial protection and sluggish ion transport. These electrochemically assembled interphases effectively address intrinsic limitations of vanadium–based AZIBs by performing multiple critical roles: (1) The layered structure facilitates continuous ion migration pathways and reducing Zn^{2+} transport energy barriers and improving cycling reversibility; (2)

the stable and uniform protective layer suppresses electric field inhomogeneities and vanadium dissolution; and (3) the abundant high–valence V^{5+} species supply additional electroactive sites, substantially enhancing the electrode's overall capacity. Simultaneously, VO_2 undergoes electrochemical reconstruction into $V_2O_5{\cdot}nH_2O$ at approximately 1.5 V, accompanied by a transition from V^{3+}/V^{4+} to V^{4+}/V^{5+} redox couples, which enables multielectron reactions and further enhances electrode capacity.[36] Enabled by these synergistic mechanisms, the electrode achieves a remarkable initial discharge capacity of 1029 mA h g^{-1} at 0.5 A g^{-1} and retains 489 mA h g^{-1} at an ultra–high current density of 20 A g^{-1}. Importantly, the full pouch cell demonstrates both high energy density (842.8 W h kg^{-1}; 0.39 mA h cm^{-2}) and power density (14,769.5 W kg^{-1}), underscoring its potential for advanced aqueous energy storage systems. Collectively, this work introduces a controllable, electrochemically tunable self–assembly approach for high–performance AZIBs with tailored interphases capable of valence–state regulation.

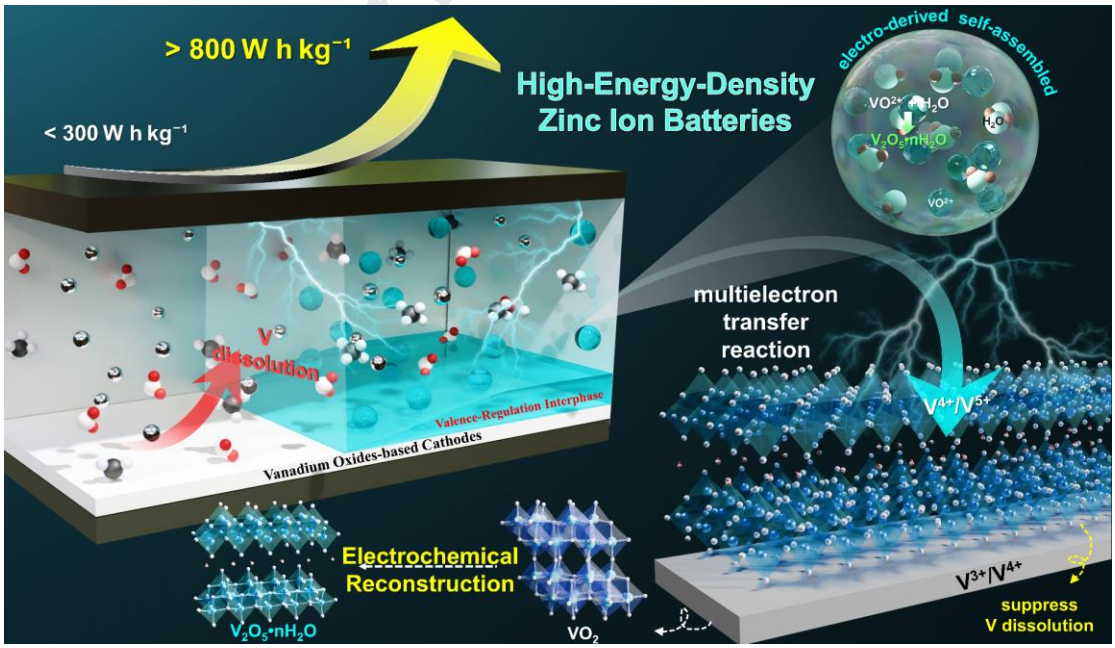

Scheme 1. Schematic illustration of the electro–driven strategy, where current–regulated self–assembly forms a dense valence–regulating interphases on the VO_2

surface, while the bulk undergoes in situ reconstruction into hydrated $V_2O_5 \cdot nH_2O$ with higher–valence vanadium. These coupled processes homogenize Zn^{2+} flux, suppress vanadium dissolution, enrich electroactive sites, and collectively enable exceptional energy and power densities in AZIBs.

2. Experimental section

2.1. Materials

Ammonium metavanadate (NH_4VO_3, ACROS ORGANICS, 99.5%), oxalic acid dihydrate ($C_2H_2O_4 \cdot 2H_2O$, Honeywell Fluka, 99.9%), vanadium (V) oxide (V_2O_5, Alfa Aesar ,99.6% min), 1–Methyl–2–pyrrolidone (NMP, anhydrous, Sigma Aldrich, 99.5%), carbon black, polyvinylidene difluoride (PVDF), zinc sulfate monohydrate ($ZnSO_4 \cdot H_2O$, Sigma Aldrich, ≥ 99.9%), vanadium (IV) sulfate oxide hydrate ($VOSO_4 \cdot xH_2O$, Thermo Scientific, 99.9%), carbon black and CR–2032 coin–type cells were acquired from Shining Energy, glass fiber was obtained from Advantec, deionized water (Millipore Milli–Q, resistivity ≥ 18.2 MΩ cm^{-1}) was used in all our experiments. All chemicals were of analytical grade and were used as received without purification unless otherwise specified.

2.2. Material characterization

The structural evolution and composition were identified using X–ray diffraction (XRD, Bruker, D8 ADVANCE) with Cu–Kα radiation (λ = 1.54 Å) and the oxidation states of the samples were characterized by high–resolution X–ray photoelectron spectrometer (XPS, ULVAC–PH, PHI QuanteraII, NTHU). All the spectra obtained from XPS analysis were first calibrated by referencing the standard binding energy of C 1 s (284.8 eV), followed by the curve fitting using the software of XPSPEAK VER. 4.1. All materials were characterized by using scanning electron microscopy (SEM, HITACHI–SU8010). Transmission electron microscopy (TEM, JEOL, JEM–

ARM200FTH), thermogravimetric analysis（TGA/DSC, Mettler–Toledo, 2–HT） and time‑of‑flight secondary ion mass spectrometer (TOF–SIMS, ION–TOF, TOF–SIMS V) were provided by NTHU services. To obtain high–resolution TEM (HRTEM) images of materials, an accelerating voltage of 200 kV was used to investigate further structure analysis including morphology, energy–dispersive spectroscopy (EDS), selected area electron diffraction (SAED), and HRTEM. UV–vis spectra were measured using an UV–vis spectroscopy (Perkin–Elmer, Lambda 35). Functional groups are observed by Fourier–transform infrared spectroscopy (FTIR, Thermo). The oxygen vacancies and unpaired electrons were characterized by electron paramagnetic resonance (EPR) spectrometer (Bruker, ELEXSYS E–580, NTHU). The confocal Raman microscope are used for pristine materials (PTT, MRID). Surface roughness was characterized by using scanning probe microscope system (AFM, Park NX–10, NCHU). Contact angle measurements were conducted using a First Ten Angstroms FTA–1000B contact angle meter at NCHU.

2.3. Preparation of Ov–VO_2

The O_v–VO_2 was synthesized by the reaction of NH_4VO_3 powder with $H_2C_2O_4$ under hydrothermal conditions. 2 mmol of NH_4VO_3 was added to 15 mL of deionized water in a water bath at 80℃ and stirred to a light–yellow color as liquid A. At the same time, 3 mmol $H_2C_2O_4$ was added to 15 mL of deionized water and stirred for 30 min as liquid B. The resultant mixture was poured into a 50 mL Teflon–lined autoclave and heated for 24 h at 180℃ after stirring to homogenous. The precipitate was collected by centrifugation and washed with deionized water and ethanol several times and dried under vacuum at 80℃ for 12 h to obtain O_v–VO_2 powder.

2.4. Electrochemical measurement

The electrochemical performance of the electrodes was tested in the CR2032 coin–type cells with the zinc metal foil (thickness: 25 μm; diameter: 15 mm) as the counter electrode. The cathode slurry consisted of VO_2, acetylene black, and PVDF in a weight ratio of 7:2:1, coated to a thickness of approximately 200 μm on carbon paper. The VO_2 loading on the cathode was 1.2–1.5 mg (≈1.1–1.3 mg cm^{-2}), corresponding to an areal current density of ≈0.49 mA cm^{-2} at 0.5 A g^{-1}, and this mass was used as the basis for specific capacity calculations. A glass-fiber separator (thickness: 0.1 mm) was used, and 150 μL of electrolyte was added per cell. The electrolyte used in the cells was 2 M $ZnSO_4 \cdot H_2O$ + 0.75 M $VOSO_4$ in DI water, with measured pH values of ≈3.7. The cells were assembled in an atmosphere environment. The cyclic voltammetry (CV) and electrochemical impedance spectroscopy (EIS) curves were obtained on Bio–Logic–Science Instruments, VMP3 workstation. Galvanostatic discharge–charge and galvanostatic Intermittent Titration Technique tests (GITT) were evaluated by NEWARE CT–4000 battery measurement system from 0.4–1.6V vs. Zn/Zn^{2+}. Operando optical microscopy (OM) observation was conducted with a customized holder (BJSCISTAR, LIB–MS–II) at 0.5 A g^{-1}.

2.5. Density functional theory (DFT) calculation

Electrostatic potential (ESP) calculations, used to visualize local charge distribution and preferred adsorption/nucleation sites, were performed using the Gaussian 16, Revision C.01 software package.[37] The hybrid functional PBE0 functional was adopted for all calculations in combination with the D3 version of Grimme's dispersion with Becke–Johnson damping (DFT–D3BJ). For geometry optimization and frequency calculations, the 6–31G+(d,p) basis set was used with the PCM solvation model for water. The single point energy calculations were performed

with 6–311+G(d,p) basis set. The diagram of ESP was visualized with the help of Multiwfn and VMD software.

3. Results and Discussion

Oxygen–deficient VO_2 (O_v–VO_2) was synthesized as a representative cathode material, and the impact of hydrothermal reaction time on its structural and defect properties was investigated to identify an optimal candidate for subsequent studies on the valence–regulation interphase. The presence of oxygen vacancies not only introduces additional active sites for Zn^{2+} intercalation/deintercalation, but also alters interfacial electron density and generates local polarization fields that lower Zn^{2+} migration barriers–collectively enhancing transport kinetics and supporting the selection of O_v–VO_2 for further investigation.[38] XRD reveals a gradual shift of the O_v–VO_2 diffraction peaks toward higher 2θ angles as the hydrothermal reaction time increases from 12 to 24 hours (**Figure 1**a, b). According to Bragg's law ($n\lambda = 2d \sin\theta$), this shift corresponds to a reduction in interplanar spacing (d), indicative of lattice contraction and improved crystallographic ordering. The prolonged hydrothermal treatment facilitates the generation of oxygen vacancies, which locally modify the V–O bonding environment and contribute to lattice contraction. These vacancies may enhance crystallographic ordering by relieving structural distortions. As a result, the O_v–VO_2 prepared under 24 hours conditions exhibit improved crystallinity and a more homogeneous distribution of oxygen vacancies, collectively contributing to a structurally stabilized and defect–engineered phase. EPR spectra confirms that the sample treated for 24 hours exhibits the highest oxygen vacancy concentration, as evidenced by an intensified signal and g–value shift, indicating abundant unpaired electrons that may serve as active sites for Zn^{2+} interaction

(Figure 1c). The evolution of surface chemistry with increasing hydrothermal duration was investigated by XPS and FTIR analyses, as shown in Figure 1d and e. XPS analysis reveals a notable increase in the proportion of V^{4+} species after prolonged treatment, indicative of enhanced oxygen vacancy formation. Concurrently, FTIR spectra confirm the presence of characteristic vibrational modes corresponding to terminal V=O (~998 cm^{-1}) and bridging V–O–V (~927 cm^{-1}) bonds, suggesting the retention of key structural motifs.

Morphological analyses conducted via SEM and TEM confirmed the formation of the characteristic tunnel–type O_v–VO_2 structure (Figure 1f, g and S1), which is structurally more stable than layered counterparts and capable of withstanding greater mechanical stress.[39, 40] Additionally, the SAED pattern displays distinct diffraction rings corresponding to the (0 1 1), ($\bar{2}$ 1 1), (2 0 0), and ($\bar{2}$ 1 3) planes of O_v–VO_2, reflecting a uniform polycrystalline structure with minimal lattice disorder (Figure 1h).[41] To confirm the uniform spatial distribution of vanadium and oxygen, STEM–EDS elemental mapping is shown in Figure 1i, showing homogeneous elemental dispersion across the O_v–VO_2 structure. HRTEM is shown as Figure 1i, revealing the presence of distinct defect regions homogeneously dispersed. Furthermore, the measured lattice spacing obtained from the FFT fitting corresponds to the (1 0 2) plane, while the observed lattice distortion and oxygen defects further validate the successful synthesis of O_v–VO_2 (Figure 1k, S2).[42] Raman spectroscopy (Figure S3) further corroborates the defect–induced modulation of vibrational bonding modes, wherein the defect–associated V–V stretching becomes most prominent in the longest–treated VO_2 sample, accompanied by a characteristic redshift of approximately 1 cm^{-1}.[43] EIS further elucidates the profound influence of oxygen vacancy concentration on charge–transfer process (Figure 1l–n). As the hydrothermal

reaction time increases, the corresponding rise in oxygen vacancy concentration within O_v–VO_2 results in a marked decrease in the imaginary component of impedance (Z'') in the low–frequency region, reflecting effective suppression of interfacial polarization. Oxygen vacancies introduce localized electronic states and undercoordinated vanadium sites, which enhance interfacial electron density, homogenize the electric field, and collectively lower polarization barriers to accelerate Zn^{2+} transport kinetics. Additionally, dielectric loss ($\tan\delta$) measurements (Figure 1n) reveal that the O_v–VO_2 sample treated hydrothermally for 24 hours exhibits the lowest dielectric loss in the high–frequency regime, indicating minimal energy dissipation under alternating current fields.[44] This reflects the suppression of non–faradaic processes, such as parasitic reactions and interfacial dipole reorganization. This phenomenon can be attributed to surface charge redistribution induced by the high concentration of oxygen vacancies, which stabilizes the interfacial electric double layer, suppresses parasitic reactions between water molecules and zinc metal, and mitigates local electric field distortions. Collectively, these effects indicate that oxygen vacancies contribute to enhanced electrochemical performance by facilitating Zn^{2+} transport and reducing interfacial polarization during cycling.

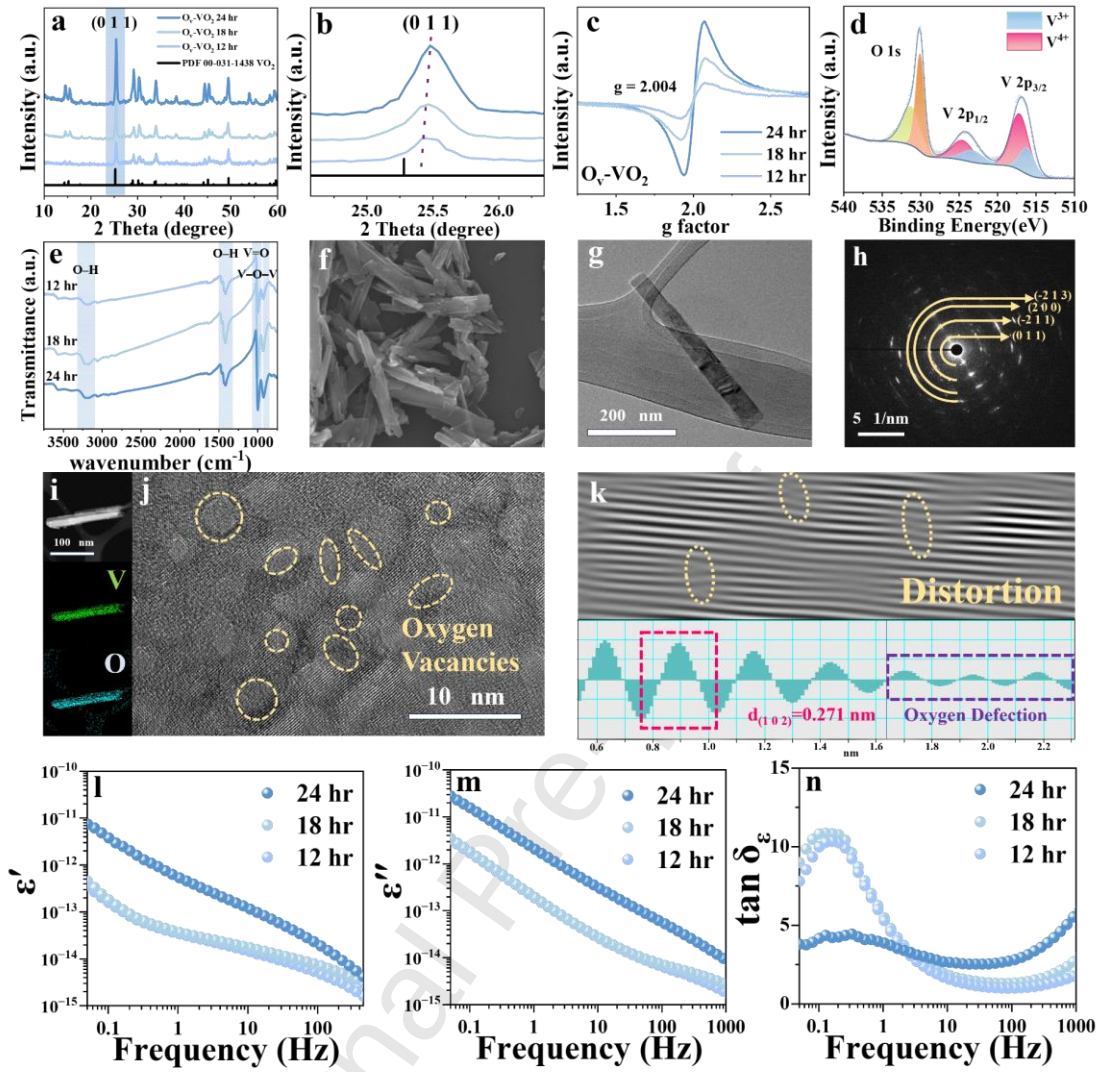

Figure 1. Structural characterization of O_v–VO_2 with different reaction times. (a) XRD patterns. (b) Enlarged (011) diffraction peak shift. (c) EPR test. (d) XPS spectra. (e) FTIR spectra. (f) SEM image. (g) TEM image. (h) SAED pattern. (i) STEM–EDS mapping of V and O elements. (j) HRTEM image with corresponding (k) FFT patterns. (l) Real part of permittivity (ε′) versus frequency. (m) Imaginary part of permittivity (ε″) versus frequency. (n) Dielectric loss (tan δ) profiles.

Given that VO^{2+} species–key to the formation of valence–regulating interphases–are introduced via the $VOSO_4$–containing electrolyte, the solution

composition significantly impacts interfacial properties such as wettability, Zn^{2+} solvation, and redox kinetics. To clarify these effects, a comparative analysis was performed between 2 M $ZnSO_4$ and 2 M $ZnSO_4$ + 0.75 M $VOSO_4$ (**Figure** 2 and S4). Firstly, contact angle measurements clearly demonstrate that electrolyte composition strongly influences interfacial wettability between the electrode and electrolyte. As shown in Figure 2a and b, contact angle measurements show that $ZnSO_4$ exhibits poor wettability on O_v–VO_2 (120.55° after 30 s), whereas the $VOSO_4$–containing electrolyte rapidly spreads (99.83°), indicating enhanced hydrophilicity and faster wetting kinetics. Hydrophilic functional groups in the additive regulate electrolyte polarity and surface tension, promoting interfacial coordination and uniform interphase growth. Beyond wettability modulation, electrostatic potential (ESP) simulations (Figure 2c and S5) suggest that $VOSO_4$ significantly reshapes the Zn^{2+} solvation environment. In $ZnSO_4$, Zn^{2+} exhibits a nearly symmetric electrostatic field arising from conventional SO_4^{2-}/H_2O coordination. By contrast, the introduction of $VOSO_4$ induces pronounced electrostatic anisotropy: localized high–potential regions reflect robust interactions between Zn^{2+} and the VO_x, while adjacent low–potential zones generate electrostatic gradients that break solvation symmetry and promote directional Zn^{2+} migration. This anisotropic potential distribution is consistent with more uniform interphase nucleation and enhanced Zn^{2+} transport kinetics. To validate this, EIS was performed after 20 cycles (Figure 2d). The introduction of $VOSO_4$ results in a pronounced shrinkage of the high–frequency semicircle in the Nyquist plot, with the real part of impedance Re(Z) decreasing from ~350 Ω ($ZnSO_4$) to ~50 Ω ($ZnSO_4$ electrolyte with $VOSO_4$). This marked reduction in internal resistance indicates that the in–situ formed interphase facilitates efficient Zn^{2+} and electron transport, thereby mitigating interfacial polarization and accelerating reaction kinetics.

Arrhenius analysis was conducted to evaluate the influence of electrolyte composition on ionic conductivity and its thermal dependence (Figure 2e). The activation energy (E_a) decreased from 33.26 KJ mol^{-1} in $ZnSO_4$ to 23.45 KJ mol^{-1} with $VOSO_4$, validating its role in enhancing ion transport and reaction kinetics.[45] Furthermore, the UV–Vis absorption spectra of these two electrolytes were compared. The emergence of a broad absorption peak at ~700 nm in the $VOSO_4$–containing electrolyte (Figure 2f) indicates the presence of VO^{2+} species, absent in pure $ZnSO_4$. These species are directly involved in initiating interphase formation during electrochemical activation. Raman spectra of the electrolyte containing $VOSO_4$ (Figure 2g) exhibit prominent features corresponding to the symmetric (ν_1, ~1020 cm^{-1}) and asymmetric (ν_3, ~1080 cm^{-1}) stretching modes of SO_4^{2-}. Additionally, a distinct peak at ~980 cm^{-1}, attributed to the symmetric stretching vibration of the V=O bond, confirms the incorporation of $VOSO_4$ into the electrolyte. To further elucidate how electrolyte composition affects the formation of the interphase during cycling, in–situ optical microscopy (OM) was employed to directly visualize electrode surface evolution throughout the first charge–discharge cycle (Figure 2h and Videos S1–S2). In the pure $ZnSO_4$ electrolyte, the electrode surface remained largely unchanged, suggesting the absence of the interphase formation. In contrast, the $VOSO_4$–containing electrolyte induced a progressive color change (dark green) across the electrode surface during charging, accompanied by a noticeable increase in thickness, indicative of the electrochemically driven nucleation and growth of an interphase. Notably, Figure 2i schematically illustrates the electro–driven self–assembly process, wherein electrolyte–derived VO^{2+} species coordinate with H_2O molecules to initiate controlled interphase nucleation at the cathode surface. Under optimized current regulation, this self–assembly proceeds in an orderly manner, guiding the growth of

uniform and compact interphases. Such interfacial modulation facilitates Zn^{2+} transport and substantially enhances the overall electrochemical performance.

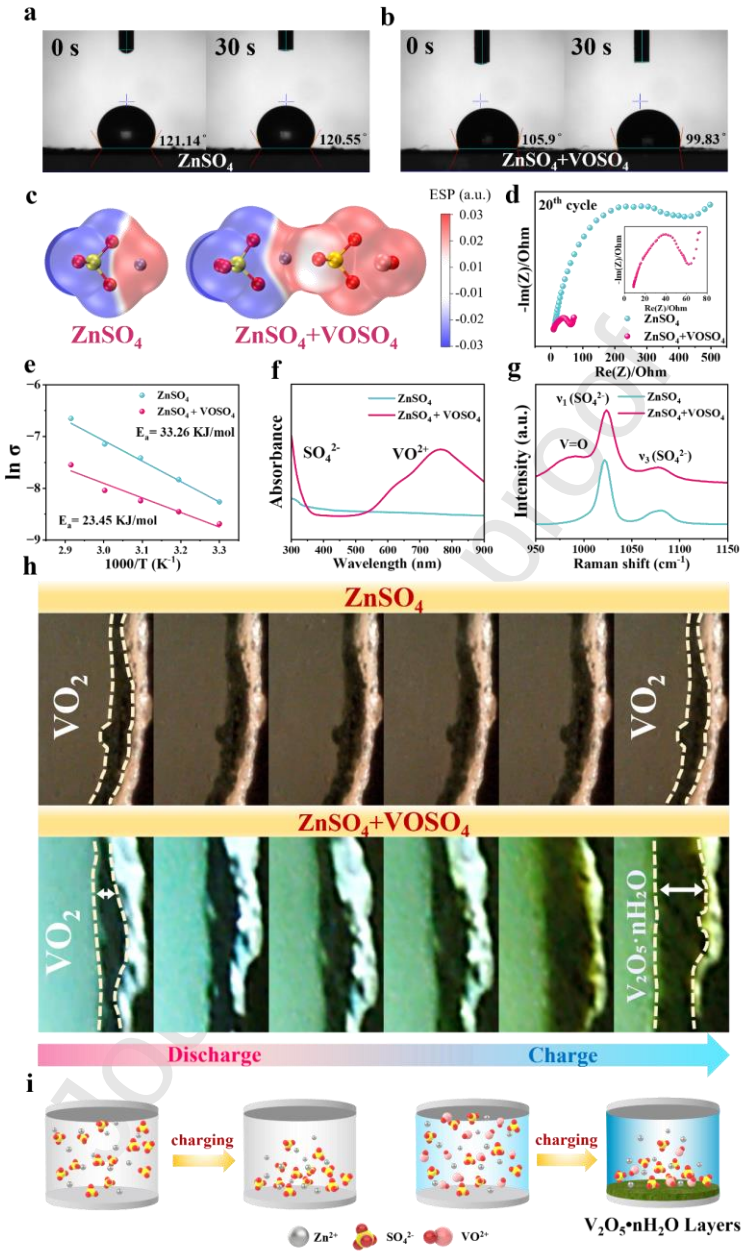

Figure 2. Comparison with and without $VOSO_4$ in $ZnSO_4$ electrolyte. (a–b) Contact angle measurements at 0 and 30 s. (c) Electrostatic potential maps. (d) EIS after cycling 20th cycle. (e) Arrhenius plot. (f) UV–vis spectra. (g) Raman spectra. (h) In–situ OM observation. (i) Schematic illustration of the interphase formation.

The self–assembly process, modulated by current–controlled kinetics, dictates the nucleation rate and growth uniformity of the interphase, with faster and slower activation dynamics yielding markedly different morphologies and uniformities. **Figure** 3 presents a comprehensive microstructural and surface characterization of O_v–VO_2 electrodes before and after the first–cycle electrochemical activation under current densities of 0.5 A g^{-1} and 0.1 A g^{-1}, respectively, elucidating the impact of activation conditions on the formation and uniformity of the electro–driven valence–regulating interphase. TEM and SEM images (Figure 3a, b and S6) reveal that the sample activated at 0.5 A g^{-1} facilitates the formation of a compact, continuous, and well–adhered interphase with an average thickness of approximately 10 nm. In contrast, the protective layer generated under 0.1 A g^{-1} activation (Figure 3c, S7 and S8) displays a loosely packed and non–uniform morphology, primarily due to limited mass transport and spatially heterogeneous reaction kinetics during the activation process.[18] The morphological irregularity and structural inconsistency give rise to uneven active site distribution and localized field intensification, increasing Zn^{2+} migration barriers and promoting side–product accumulation, thereby destabilizing interfacial reactions and reducing cycling efficiency.[46] AFM was employed to quantitatively assess surface morphology and topographical uniformity (Figure 3d–i and S9-10). The sample activated at 0.5 A g^{-1} exhibit a smoother and more homogeneous surface profile with significantly reduced surface fluctuations, indicating improved structural ordering and low surface roughness.[47] The corresponding surface roughness parameter (R_a) further exhibits a notable disparity. For the sample activated at 0.5 A g^{-1}, the averaged R_a obtained from multiple AFM scan regions was 36.6–43.9 nm, substantially smaller than that of the 0.1 A g^{-1} sample (109.6–112.9 nm) and the inactivated Ov–VO_2 electrode (≈335 nm; Figure 3g–i).

These results highlight the role of higher activation current in directing self–assembly, reducing roughness, and ensuring uniform Zn^{2+} transport pathways. To further elucidate the influence of interphase uniformity on surface stress distribution and electric field homogenization, finite element method (FEM) simulations were employed to analyze von Mises stress and electric field distributions, as illustrated in Figure 3j. As shown in the von Mises stress mapping (Figure 3j), the sample activated at 0.5 A g^{-1} exhibits a relatively uniform stress distribution, with maximum stress localized centrally and minimal fluctuations across the surface, suggesting effective stress dissipation and enhanced mechanical stability.[48] In contrast, the sample activated at 0.1 A g^{-1} displays pronounced stress concentrations associated with surface irregularities and non–uniform interphases formation. Similarly, electric field simulations (Figure 3k–l and S11) indicate that uniform interphases formed at 0.5 A g^{-1} are associated with a more vertically aligned Zn^{2+} flux distribution, whereas non-uniform interphases formed at 0.1 A g^{-1} result in pronounced field distortion and localized Zn^{2+} accumulation.[49] Taken together with the experimental observations, these results support the view that fast-kinetics activation at 0.5 A g^{-1} is associated with the formation of more uniform valence-regulating interphases, accompanied by improved Zn^{2+} flux uniformity, reduced stress and electric-field heterogeneity, and enhanced cycling reversibility.

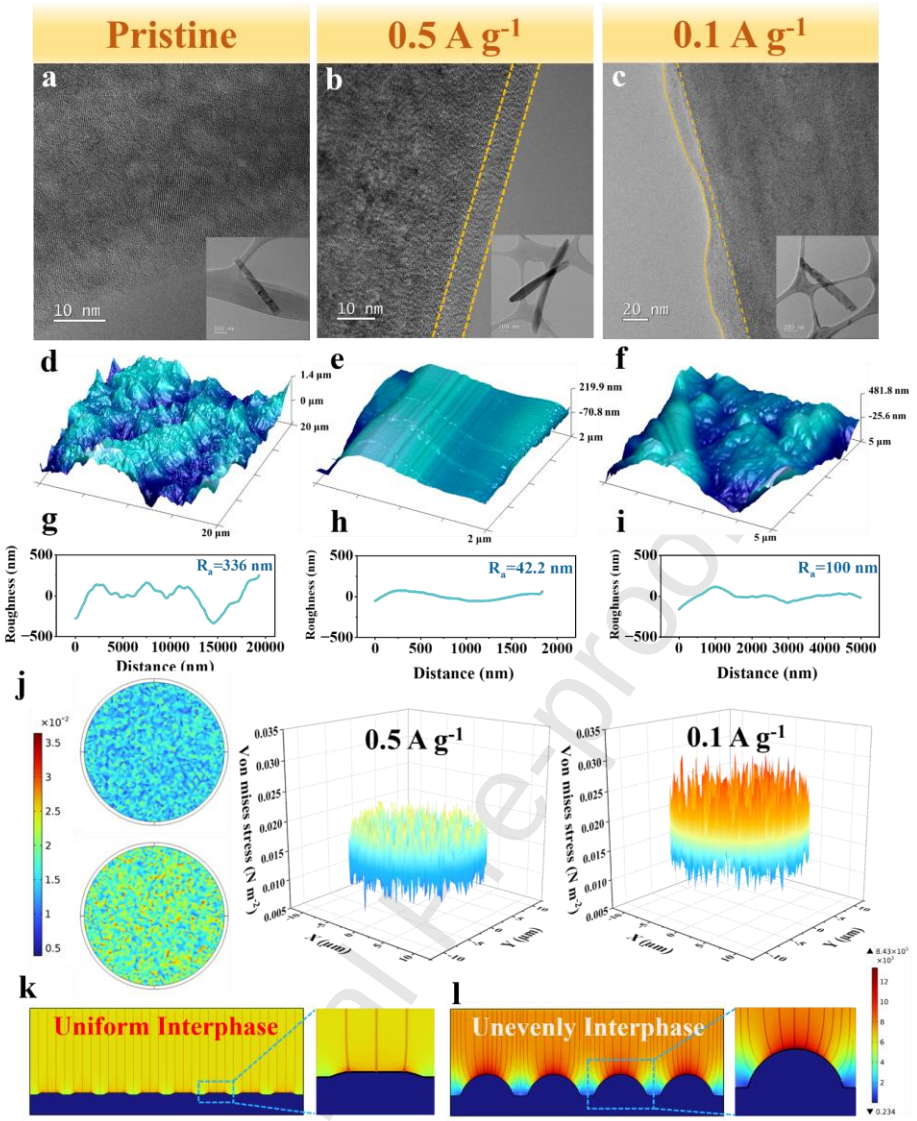

Figure 3. Structural and simulation analyses of interphase generated under different electrochemical activation conditions. (a–c) HR–TEM images. (d–f) 3D AFM images. (g–i) Corresponding average surface roughness (R_a). (j) COMSOL simulation of von Mises stress distributions. (k–l) COMSOL simulation of electric field intensity profiles.

Figure 4 employs multiple in–situ characterization methods to resolve the cathodic valence–state transition pathway and concurrent VO_2 reconstruction under electro–driven activation. In–situ and ex–situ XRD results (Figure 4b and S12) reveal

the emergence of $V_2O_5 \cdot nH_2O$ reflections at the initial discharge stage, confirming that interphases enriched in high–valence V^{5+} species are self–assembled early. Concurrently, progressive shifts in VO_2 diffraction peaks indicate Zn^{2+} intercalation. Upon subsequent charging, a distinct voltage plateau appears at ~1.5 V (Figure 4a), accompanied by a strong diffraction peak at 23.8°, consistent with electrochemical reconstruction into layered $V_2O_5 \cdot nH_2O$.[16, 50] Moreover, no diffraction features associated with $Zn_3(OH)_2V_2O_7 \cdot 2H_2O$ are detected under $VOSO_4$-assisted conditions (Figure S13), indicating that the electrolyte-derived interphase helps suppress the formation of this inactive byproduct during cycling. This dual evolution–interphase assembly and VO_2 oxidation–establishes a stable, valence–regulating interface that enhances Zn^{2+} kinetics and cycling durability. Complementary ex–situ FTIR and TGA analyses (Figure S11–13) confirm the additive–induced hydrated interphase, as evidenced by characteristic V=O and H–O–H vibrations and enhanced thermal water loss. TGA analysis (Figure S14-17) further confirms that the crystal water within $V_2O_5 \cdot nH_2O$ remains stable during long-term cycling. High–resolution TEM and STEM–EDS elemental mapping (Figure 4c–h and S18–23) provides direct structural evidence for interphase evolution. In the electrolyte without $VOSO_4$ additive, the VO_2 surface exhibits no interfacial layer formation, in sharp contrast to the lamellae observed in the $VOSO_4$–containing system. This comparison demonstrates the role of $VOSO_4$ in triggering interphase self–assembly and promoting the early–stage evolution of ordered, multilayered structures. The phase transition was further monitored by in–situ Raman spectroscopy (Figure S24). During cycling, the attenuation of VO_2–associated peaks, together with the sustained prominence of the ~500 cm^{-1} V–O–V band (characteristic of $V_2O_5 \cdot nH_2O$), provides evidence not only for the structural reconstruction of VO_2 into $V_2O_5 \cdot nH_2O$ but also for the concurrent

formation of V^{5+}–rich interphases.[43, 51] The spatial distribution of this transformation was further visualized by TOF–SIMS 3D mapping (Figure 4j), comparing electrodes at different charge–discharge states: (i) discharged to 0.4 V (D0.4), (ii) charged to 1.4 V (C1.4), and (iii) charged to 1.6 V (C1.6). With progressive activation, V_2O_5 signals (pink) intensify and become more uniformly distributed, while VO_2 signals (blue) diminish, indicate progressive VO_2 oxidation accompanied by the formation of V^{5+}–rich interphases. These observations correlate with the charge plateau (Figure 4a) and Raman spectra (Figure 4i), reinforcing the linkage between electro–driven valence–state regulation and interphase assembly. To gain further insight into the valence state evolution during cycling, ex–situ XPS analysis (Figure 4i and S25) provides direct evidence at the electronic structure. The deconvolution of V 2p peaks shows a clear increase in the V^{5+}/V^{4+} ratio during charging, rising from 0.71 at OCP to 4.9 at 1.6 V, evidencing substantial oxidation. This progressive $V^{4+}\rightarrow V^{5+}$ transition indicates that valence regulation occurs within the interphase during electrochemical activation. [13] To validate the importance of the ~1.5 V plateau, the voltage window was restricted to 0.4–1.4 V (Figure S26–28). Without reaching the activation plateau, interphase growth was suppressed and cell performance deteriorated markedly. These analyses confirm that $VOSO_4$ facilitates the electrochemically driven self–assembly of valence–regulating interphases during the initial activation. The combined effects of electrochemical reconstruction and V^{4+}/V^{5+} oxidation give rise to a homogeneous V^{5+}–enriched interphase that facilitates Zn^{2+} transport, enhances interfacial charge–transfer kinetics, and ensures durable cycling stability.

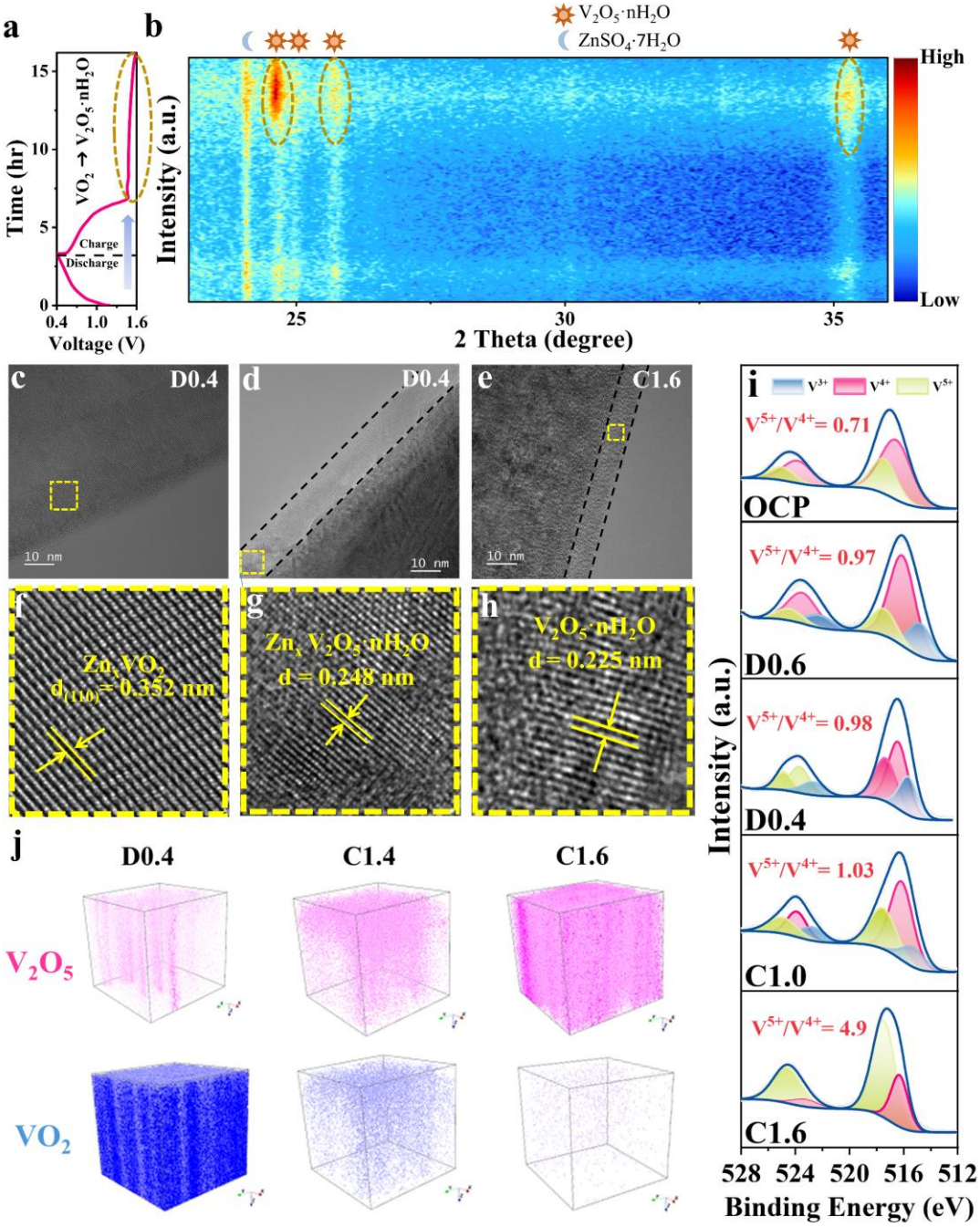

Figure 4. Mechanism of structural evolution during the first cycle. (a–b) In–situ XRD patterns. HR–TEM images of electrodes at specific charge–discharge potentials: (c) D0.4 (discharged to 0.4 V) without $VOSO_4$, (d) D0.4 (discharged to 0.4 V) with $VOSO_4$, (e) C1.6 (charged to 1.6 V) with $VOSO_4$. (f–h) Corresponding magnified views of (c–e), respectively. (i) Ex–situ XPS spectra. (j) 3D TOF–SIMS of V_2O_5 and VO_2 phases.

Activation under controlled fast– (0.5 A g^{-1}) and slow–kinetics (0.1 A g^{-1}) conditions yields markedly different electrochemical behaviors, reflecting the critical role of current–directed interphase formation (**Figure** 5). CV profiles obtained at a scan rate of 0.5 mV s^{-1} within 0.4–1.6 V exhibit two distinct pairs of redox peaks, reflecting the multi–step redox processes involved (Figure 5a and S29). A gradual increase in peak current with successive scans indicates progressive activation and enhanced electrochemical reactivity (Figure 5a).[10] Notably, under identical scan rates, the electrode activated at 0.5 A g^{-1} delivers markedly higher peak currents than that at 0.1 A g^{-1}, confirming superior redox activity and faster kinetics (Figure 5b). This enhancement is attributed to the electro–driven self–assembly of uniform valence–regulating interphases, which provide abundant electroactive sites, homogenize interfacial electric fields, and suppress polarization.[52] Moreover, a strong anodic peak around 1.5 V in the first cycle corresponds to the electrochemical activation plateau and the VO_2 → $V_2O_5{\cdot}nH_2O$ transition, enriching the electrode surface with high–valence V^{5+} species that further promote reversible Zn^{2+} storage.[53, 54] Analysis of the differential capacity (dQ/dV) curves reveals a distinct oxidation peak within 1.4–1.5 V for both activation currents, associated with the V^{3+}/V^{4+} → V^{4+}/V^{5+} transition and the establishment of V^{5+}–rich interphases (Figure S30 and S31).[32] The peak is more intense and better resolved at 0.5 A g^{-1}, reflecting faster activation kinetics and more uniform interphase formation. This process is consistent with the previously identified VO_2 → $V_2O_5{\cdot}nH_2O$ reconstruction, with TEM and AFM observations further revealing that interphases form in both cases but with markedly different uniformity depending on the activation current density. Figure 5c shows the dQ/dV profiles after 20 cycles, highlighting the impact of activation

conditions on long–term reaction behavior. Both electrodes exhibit dual peaks at ~0.6 V and ~1.0 V, typical of vanadium–based systems.[1, 15, 52] However, the 0.5 A g^{-1}–activated electrode retains a much stronger redox response at ~0.6 V, reflecting the role of a uniformly self–assembled valence–regulating interphase in sustaining efficient Zn^{2+} transport and reversible electron transfer. By contrast, the 0.1 A g^{-1} electrode shows attenuated signals, consistent with interfacial heterogeneity and sluggish kinetics. This is consistent with the stable 0.6 V plateau in the galvanostatic charge–discharge (GCD) curves (Figure S32). Further insights are obtained from the first–cycle charging behavior (Figure 5d). At 0.1 A g^{-1}, an abnormally high first–charge capacity (~5000 mA h g^{-1}) arises due to sluggish kinetics and insufficient driving force, which cause uneven interphase growth and excessive charge accumulation. The resulting defective interphase promotes over–oxidation, side reactions, and irreversible capacity buildup. By contrast, activation at 0.5 A g^{-1} drives self–assembly of the valence–regulation interphase, buffering volume changes during Zn^{2+} cycling, and ensuring stable and reversible redox processes.

When comparing activation conditions, the electrode activated at 0.5 A g^{-1} exhibits an initial discharge capacity above 1000 mA h g^{-1} (0.97 mA h cm^{-2}) and retains ~600 mA h g^{-1} (0.584 mA h cm^{-2}) after 500 cycles (Figure 5e, f). In contrast, the 0.1 A g^{-1}–activated electrode experiences rapid capacity decay to ~200 mA h g^{-1} (0.194 mA h cm^{-2}) within 100 cycles. GCD profiles after 50 and 100 cycles show that the low–current sample suffers severe plateau fading and increased overpotential, while the high–current sample retains stable plateaus with minimal polarization (Figure S33). Figure 5f demonstrates that after the activation process, the electrode activated at 0.5 A g^{-1} exhibits a significantly higher capacity retention compared to that activated at 0.1 A g^{-1}, highlighting the beneficial effect of higher–current

activation on stabilizing long–term cycling performance. These differences stem from the distinct interphase structures formed during activation, with the 0.5 A g^{-1} condition producing a more uniform and ion–conductive layer that facilitates Zn^{2+} transport and stabilizes redox reactions. The rate capability results (Figure 5g) confirm stable performance across 0.5–20 A g^{-1}, with specific capacities of 1025 , 910, 797, 717, 622, 546, and 489 mA h g^{-1}, respectively. When the current density returns to 0.5 A g^{-1}, capacity recovery to near–initial values further highlights the structural reversibility of the self–assembled interphase. High–rate cycling tests further demonstrate the robustness of the optimized interphase (Figure 5h, S34). At 20 A g^{-1}, the 0.5 A g^{-1}–activated electrode delivers an initial capacity of 540 mA h g^{-1} (0.457 mA h cm^{-2}) and retains 345.6 mA h g^{-1} (0.336 mA h cm^{-2}) after 1000 cycles, indicating excellent tolerance to fast ion kinetics. Remarkably, even under both low (0.5 A g^{-1}) and ultrahigh (20 A g^{-1}) current densities, the electrode achieves superior specific capacities, clearly surpassing previously reported vanadium–based cathodes (Figure i and Table S1).[1, 55-59] Additionally, the general applicability of this electro–driven self–assembly strategy was validated on other vanadium–based cathodes, including V_2O_5, V_2O_3, and $NH_4V_4O_{10}$ (Figure 5j, S35–S38). In all cases, initial activation produced a distinct 1.4–1.5 V plateau associated with V^{4+}/V^{5+} evolution, indicating the formation of V^{5+}–rich interphases and confirming the strategy's universality for enhancing Zn^{2+} storage kinetics and interfacial stability across diverse vanadium oxides (Figure 5k).[54, 60, 61] Compared with conventional VO_x optimization schemes such as metal doping, this method delivers superior rate capability (Table S2).[62-65] This superior high–rate durability highlights the robustness of the electro–driven self–assembly strategy in facilitating fast Zn^{2+} storage kinetics.

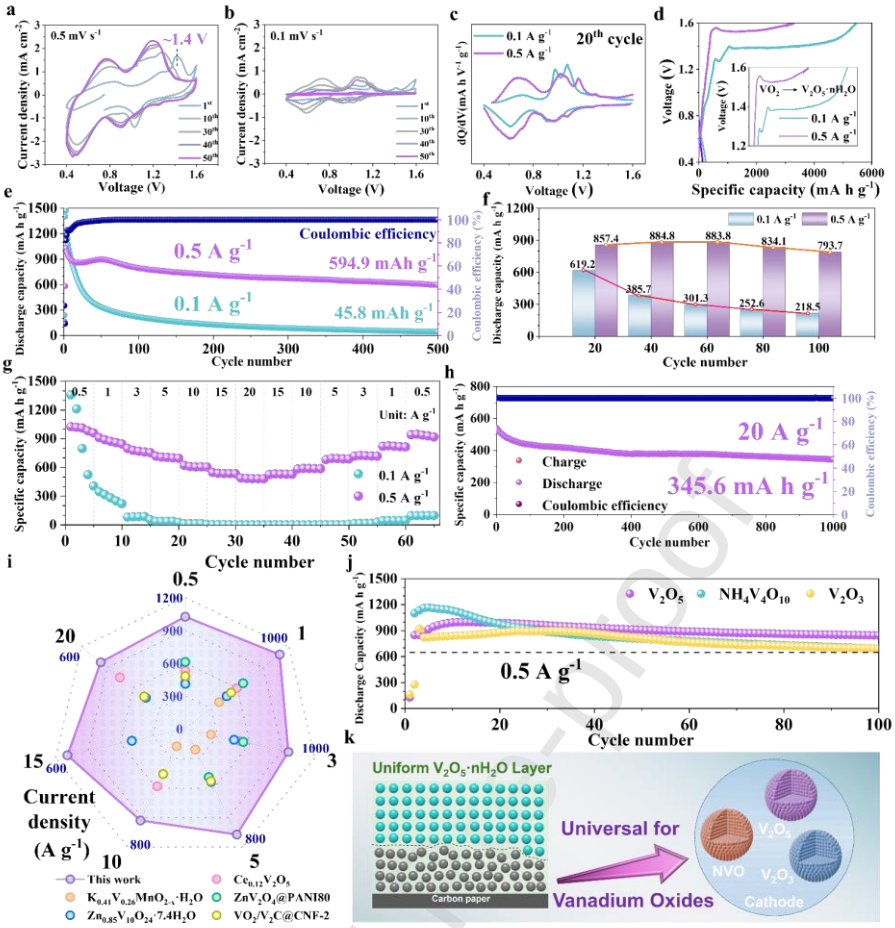

Figure 5. Electrochemical performance under different current densities. (a, b) CV curves at 0.5 mV s^{-1} and 0.1 mV s^{-1}. (c) dQ/dV comparison at the 20th cycle for both current densities. (d) GCD curves of the first cycle and (e) cycle performance at 0.5 A g^{-1} and 0.1 A g^{-1}. (f) Discharge capacity with different cycle between 0.5 A g^{-1} and 0.1 A g^{-1}. (g) Rate performance. (h) Cycle performance at 20 A g^{-1}. (i) Comparison of rate performance between this work and previously reported vanadium–based cathode materials. (j) Cycle performance at 0.5 A g^{-1} of different vanadium oxides cathodes. (k) Schematic illustration of the vanadium–based cathodes in $ZnSO_4$ electrolyte with $VOSO_4$.

To investigate the influence of the electro–driven self–assembled interphase on the reaction kinetics of O_v–VO_2, a suite of electrochemical analyses–including CV, galvanostatic intermittent titration technique (GITT), in–situ EIS, and capacitive/diffusion contribution deconvolution–was employed (**Figure** 6). As illustrated in Figure 6a, the CV curves obtained within a scan rate range of 0.2–1.0 mV s^{-1} exhibit multiple well–defined and highly reproducible redox peaks, indicative of the reversible redox behavior of O_v–VO_2. With increasing scan rate, anodic and cathodic peak currents grow proportionally, reflecting accelerated charge–transfer kinetics. The persistence of well–defined redox peaks without significant broadening at high scan rates suggests that the interphase maintains reversible Zn^{2+} transport and mitigates interfacial polarization.[66, 67] To further reveal the underlying charge storage behavior, log(i)–log(v) analyses were performed, as shown in Figure 6b. The b–value analysis reveals that the storage process is predominantly governed by surface–controlled capacitive behavior, as indicated by b–values of 0.814, 0.79, and 0.98 for peaks 1, 2, and 4, respectively. A moderate diffusion–controlled contribution is observed at peak 3 (b = 0.597). This hybrid capacitive–diffusion mechanism is further supported by capacitive contributions increasing from 40% to 59% with scan rate (Figure 6c and S39), highlighting the role of the valence–regulation interphase in boosting surface–dominated kinetics and facilitating rapid Zn^{2+} transport.[36, 68] To evaluate the impact of activation conditions on Zn^{2+} diffusion kinetics, GITT tests were conducted on electrodes activated at 0.5 and 0.1 A g^{-1} for 20 cycles (Figure 6d , e and S40). The electrode activated at 0.5 A g^{-1} exhibited diffusion coefficients (D_{Zn2+}) ranging from 10^{-6} to 10^{-9} cm^2 s^{-1} with low overpotentials, evidencing efficient ion transport and minimal polarization.[38, 69] Conversely, the electrode activated at 0.1 A g^{-1} showed sluggish kinetics, with

broader D_{Zn2+} values (10^{-7}–10^{-11} cm^2 s^{-1}) and pronounced overpotentials, attributable to non–uniform interphase formation that disrupts homogeneous Zn^{2+} transport [70] The averaged D_{Zn2+} values further highlight these differences, with the sample activated at 0.5 A g^{-1} exhibiting a narrower D_{Zn2+} distribution and consistently higher values during both discharge (1.19×10^{-8} cm^2 s^{-1}) and charge (1.06×10^{-7} cm^2 s^{-1}). These results demonstrate that applying electro-driven activation at 0.5 A g^{-1} yields a more uniform $V_2O_5 \cdot nH_2O$ interphase, which facilitates Zn^{2+} transport throughout cycling. Impedance analyses corroborate these findings. As shown in Figure S41, the electrode activated at 0.5 A g^{-1} displays markedly lower charge–transfer resistance, with a smaller high–frequency semicircle compared to the 0.1 A g^{-1} electrode. In–situ EIS was recorded at different states of charge during the second cycle to track interfacial impedance evolution (Figure 6f and g). Under 0.5 A g^{-1} activation, the electrode consistently maintains a low real impedance (Re(Z) < 100 Ω), reflecting efficient charge transfer and a robust, electrochemically adaptive interphase.[71-74] In contrast, the 0.1 A g^{-1} sample exhibits high initial impedance (~1000 Ω) and marked fluctuation, suggesting that non–uniform interfaces and localized transport bottlenecks. Corresponding of relaxation times (DRT) analysis, used to deconvolute EIS spectra into distinct kinetic processes, revealed rate–dependent impedance behavior. At 0.5 A g^{-1} (Figure 6h), a uniform and continuous $V_2O_5 \cdot nH_2O$ coating ensures low resistance with only short–to–medium τ signals, and impedance further decreases beyond ~1.2 V. In contrast, at 0.1 A g^{-1} (Figure 6i), the non–uniform distribution of $V_2O_5 \cdot nH_2O$ gives rise to a pronounced long τ peak (~0.8–1.2 V) and sustained high resistance, reflecting aggravated polarization and compromised interfacial stability.[75] These findings demonstrate that optimized current regulation enables uniform valence–regulating interphases that simultaneously stabilize ion

transport and govern valence–state transitions, thereby ensuring fast Zn^{2+} kinetics and minimizing polarization.

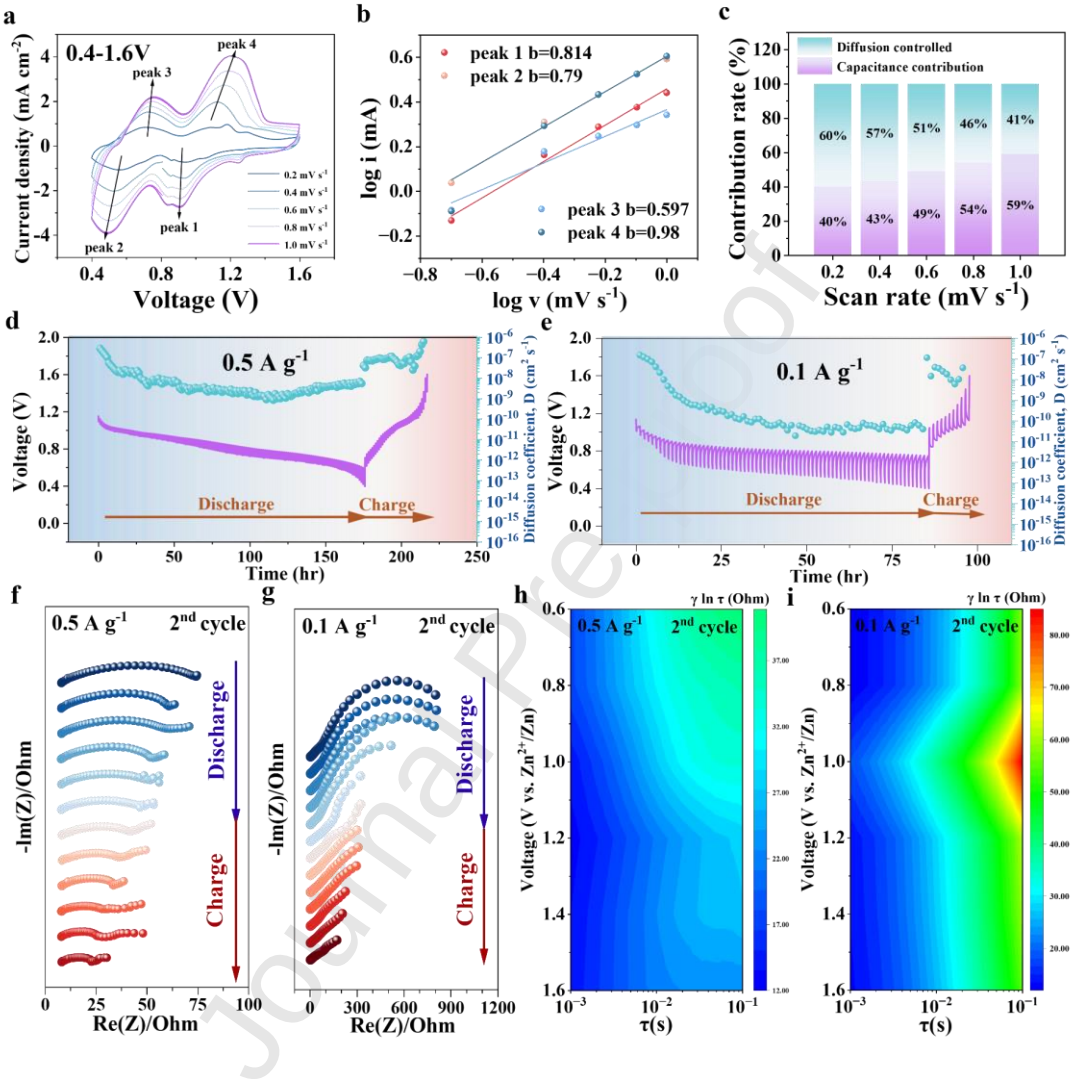

Figure 6. Kinetics analysis under different activation conditions. (a) CV curves at different scan rates and (b) corresponding b–value. (c) Diffusion and capacitance contribution ratio. GITT profiles obtained at (d) 0.5 A g^{-1} and (e) 0.1 A g^{-1}. In–situ EIS profiles of 2nd cycle at (f) 0.5 A g^{-1} and (g) 0.1 A g^{-1}. DRT results of R_{ct} for 2nd cycle charge process in (h) 0.5 A g^{-1} and (i) 0.1 A g^{-1}.

The structural reversibility of the interphase formed during electrochemical activation is pivotal for long–term cycling stability and capacity retention. After 20 cycles, ex–situ TEM images (**Figure** 7a, b) clearly reveal that the electrodes activated at 0.5 A g^{-1} exhibit a conformal and continuous ion–conducting interfacial layer, indicative of excellent structural reversibility. The preserved morphology confirms that the self–assembled V^{5+}–rich layer remains mechanically and chemically stable under repeated Zn^{2+} intercalation/deintercalation, effectively accommodating volumetric strain and preventing stress–induced failure.[76] In contrast, the electrode activated at 0.1 A g^{-1} (Figure 7c, d) exhibits a non–uniform protective layer with fluctuating thickness and pronounced boundary irregularities. This heterogeneity promotes localized electric field enhancement and obstructed ion transport, leading to interfacial instability and deteriorated electrochemical performance upon cycling. To further quantify surface uniformity, 3D AFM scans and surface roughness (R_a) measurements were performed, as shown in Figure 7e, f, S42 and S43. The electrode activated at 0.5 A g^{-1} shows a smooth surface with a low roughness (R_a = 171 nm), increasing only modestly from its initial value (42.2 nm), whereas the electrode activated at 0.1 A g^{-1} displays severe topographic distortion (R_a = 748 nm, from 100 nm initially), highlighting the instability of non–uniform interphases and their inability to maintain smooth Zn^{2+} transport pathways.[77] SEM observations after 20 cycles (Figure S44 and S45) show intact surfaces at 0.5 A g^{-1} but crack formation at 0.1 A g^{-1}, confirming the instability of non–uniform interphases. High–resolution XPS analysis provides deeper insights into the dynamic valence behavior during the second cycle (Figure 7g and h). The spectra confirm that V^{5+} remains the dominant component throughout both discharge and charge, with only slight shifts in the V^{5+}/V^{4+} ratio. A minor reduction from V^{5+} to V^{4+} occurs during Zn^{2+} insertion and is

largely reversed during extraction, reflecting reversible modulation of vanadium valence states.[78] This behavior highlights the interphase's dual role: not only structurally stable but also electrochemically adaptive, actively regulating valence states to stabilize Zn^{2+} storage. To assess long–term interfacial stability, in–situ EIS was conducted during the 20^{th} cycle (Figure S46). The Nyquist plots exhibit consistently low real impedance (Re(Z) ≈ 50–80 Ω), reflecting minimal polarization.[79] This result is attributed to the ordered structure and strong adhesion of the electro–driven interphase, which maintains selective Zn^{2+} transport and suppresses interfacial degradation. Furthermore, post–cycling 3D TOF–SIMS mapping of V species and COMSOL simulations of Zn^{2+} concentration profiles (Figure 7i, j, S47 and S48) reveal distinct differences in interphase uniformity and ion transport behavior. In the 0.5 A g^{-1}–activated sample, a uniform V_2O_5 distribution and smooth Zn^{2+} flux are observed, validating the stability of the self–assembled interphase. Conversely, the sample activated at 0.1 A g^{-1} exhibited exhibits fragmented or strip–like V signals, accompanied by uneven Zn^{2+} accumulation and spatially intensified reactions, which accelerate interfacial degradation. These post–cycling analyses confirm that only the uniformly self–assembled interphase (0.5 A g^{-1}) can withstand repeated Zn^{2+} insertion/extraction, maintaining stable ion transport pathways over extended operation.

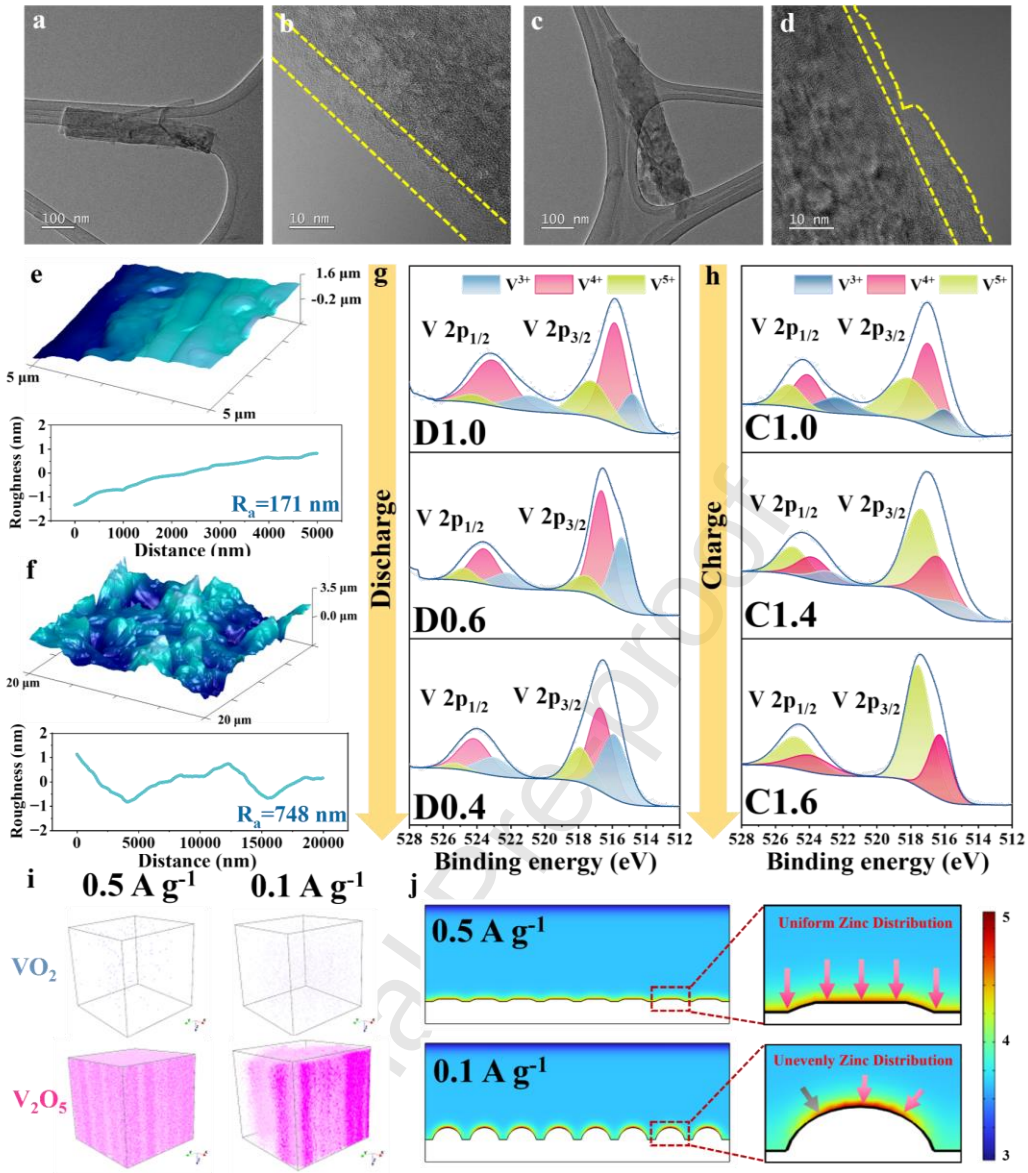

Figure 7. Post–cycling evaluation of interphase structural stability. Ex–situ TEM images after 20 cycles (a–b) at 0.5 A g^{-1} and (c–d) at 0.1 A g^{-1}. (e–f) 3D AFM images and corresponding roughness (Ra). (g–h) Ex–situ XPS spectra of V element in 2nd cycle. (i) 3D TOF–SIMS distribution. (j) COMSOL simulations of Zn^{2+} concentration distribution.

Building on the promising coin–cell results, electrochemical tests in a pouch cell configuration were conducted to evaluate the applicability of the electro–driven valence–regulation strategy (**Figure** 8a). Cycle performance at 0.5 A g^{-1} (Figure 8b)

shows an initial discharge capacity of ~1057 mA h g^{-1} (0.555 mA h cm^{-2}), with a sustained capacity exceeding 667 mA h g^{-1} after 250 cycles, accompanied by nearly 100% Coulombic efficiency. The corresponding symmetric GCD profiles (Figure S49) further corroborate the reversibility of Zn^{2+} storage, while the long–term stability can be attributed to interphase–mediated charge/ion regulation, which suppresses side reactions and maintains efficient transport pathways. Even at a high current density of 3 A g^{-1}, the cell maintains 560 mA h g^{-1} (0.266 mA h cm^{-2}) over 300 cycles (Figure 8c), demonstrating outstanding long–term durability. The successful illumination of 86 LED lights further validates the practical applicability of this approach for real–world energy devices. Figure 8d demonstrates that the electrode delivers consistently stable performance across different current densities, indicating robust rate capability. The CV curves at 0.5 mV s^{-1} exhibit negligible shifts in redox peak positions over 50 cycles, reflecting highly reversible Zn^{2+} insertion/extraction and demonstrating that the V^{4+}/V^{5+} redox reversibility is well preserved in the pouch–cell configuration (Figure 8e).[80] Moreover, the observed reduction in charge–transfer resistance (Re(Z)) after the first cycle (Figure 8f) confirms that these interphases effectively lower internal impedance and accelerate Zn^{2+} transport kinetics. The pouch cell also demonstrates remarkable rate performance (Figure 8g and S50), achieving 1054–482 mA h g^{-1} across current densities of 0.5–20 A g^{-1}, with excellent reversibility upon returning to 0.5 A g^{-1} (957 mA h g^{-1}). This stability at high rates confirms that electro–driven valence regulation effectively suppresses polarization. As shown in Figure 8h, the battery delivers an impressive energy density of 843 W h kg^{-1} at 443 W kg^{-1}. Even under an ultrahigh power density of 14,770 W kg^{-1}, it retains a substantial energy density of 361 W h kg^{-1}–far exceeding the performance degradation typically observed in conventional Zn–ion batteries

under high–rate conditions (Figure 8i and Table S3). Strikingly, the proposed pouch cell exhibits energy and power metrics that exceed those of previously reported Zn–ion systems, highlighting the effectiveness of the electro–driven valence–regulation strategy in sustaining high–energy, high–power AZIBs. [81-85] This performance demonstrates the role of electro–driven self–assembled valence–regulating interphases in sustaining high energy output under extreme power demands, making

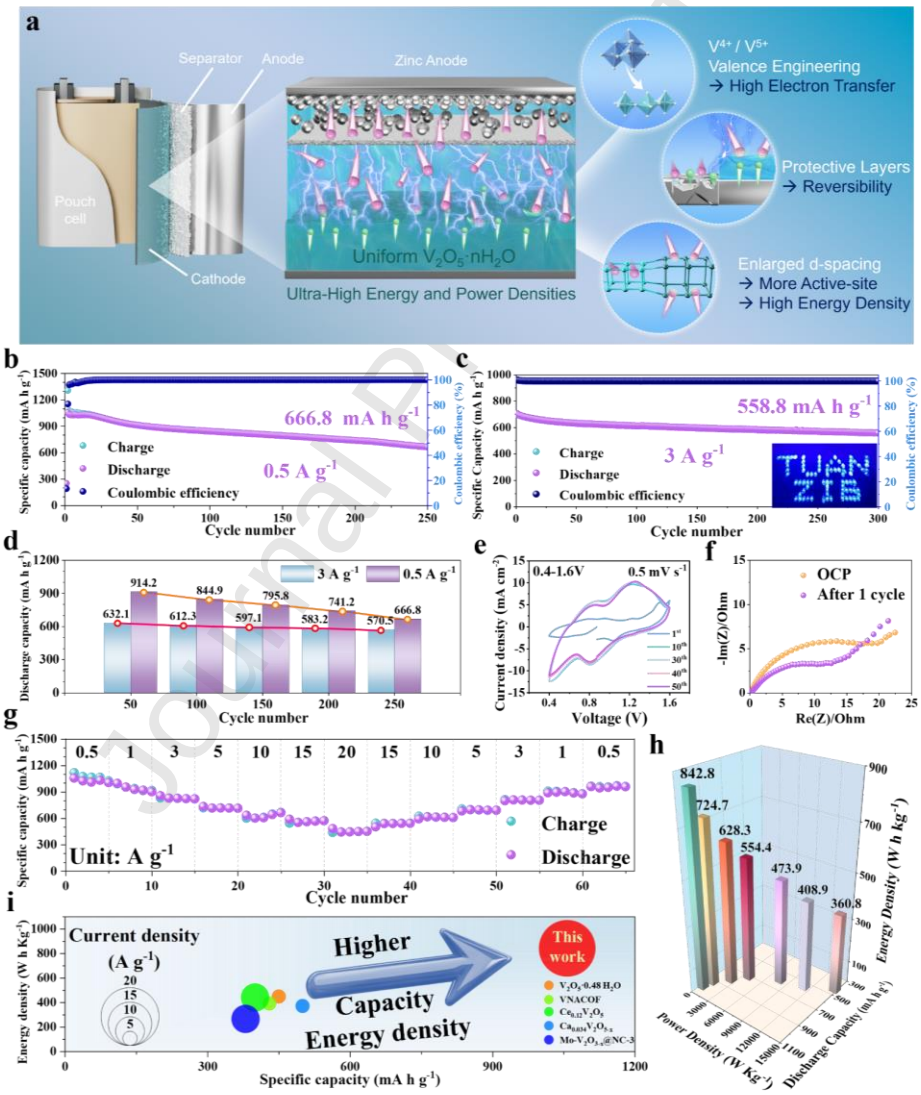

the strategy promising for high–power starter modules and portable devices.

Figure 8. Electrochemical performance of the pouch cell. (a) Schematic illustration of the Zn//VO_2 pouch cell. Cycle performance at (b) 0.5 A g^{-1} and (c) 3 A g^{-1}. (d) Discharge capacity with different cycle between 0.5 A g^{-1} and 3 A g^{-1}. (e) CV curves at 0.5 mV s^{-1}. (f) EIS test. (g) Rate performance from 0.5 A g^{-1} to 20 A g^{-1} and (h) corresponding 3D bar chart (power density, discharge capacity, energy density). (i) Comparison of the overall performance (capacity, rate, energy density and current density) between this work and previously reported vanadium–based cathode materials.

4. Conclusion

In summary, oxygen–deficient VO_2 cathodes develop adaptive interphases via electrochemically induced self–assembly, imparting the surface with selective ion conduction and dynamic valence modulation. The formation of these interphases initiates during the discharge process and becomes pronounced at the ~1.5 V charging plateau, where VO_2 undergoes electrochemical reconstruction into higher–valence vanadium phases. This dual mechanism yields both an ion–conductive interphase and a structurally adaptive, redox–active host, synergistically facilitating Zn^{2+} transport and multielectron redox reactions. Activation kinetics play a decisive role: fast–kinetics activation (0.5 A g^{-1}) promotes uniform interphase growth, suppresses interfacial polarization, and accelerates Zn^{2+} diffusion, whereas slow–kinetics activation (0.1 A g^{-1}) yields less compact, less conductive layers. The optimized 0.5 A g^{-1} condition delivers outstanding performance with high capacity (1029 mA h g^{-1}) and excellent rate capability (489 mA h g^{-1} at 20 A g^{-1}). COMSOL simulations, together with GITT and EIS analyses, support the interpretation that valence–regulating interphases contribute to reaction field homogenization and reduced ion–transport resistance. The remarkable energy and power outputs achieved in the pouch

cell (842.8 W h kg^{-1} and 14,769.5 W kg^{-1}) validate the scalability and practical relevance of this approach. More broadly, this work establishes electro–driven valence–regulating interphases as a versatile design paradigm for vanadium oxide cathodes, enabling full exploitation of their intrinsic redox flexibility and ionic transport capability toward next–generation AZIBs with integrated high–energy and high–power performance.

Data Availability Statement

The data that support the findings of this study are available from the corresponding author upon reasonable request.

Acknowledgements

This work was supported by financial support from the 2030 Cross–Generation Young Scholars Program by the National Science and Technology Council (NSTC). H.–Y. Tuan also acknowledges the financial support of National Tsing Hua University, Taiwan, through the grant of NSTC 113–2628–E–007–006 and NSTC 114–2628–E–007–003.

Conflict of Interest Statement

The authors declare no conflict of interest.

References

[1] D.–H. Liu, A. Wang, Y. Liu, F. Xu, D. Luo, J. Zheng, M. Song, C. Xu, Z. Chen, V–O–Ru Heterogeneous Interphase Reversible Reconstruction Endowing

$Zn_{0.85}V_{10}O_{24} \cdot 7.4H_2O$/0.65 RuO_2 Cathode Robust H^+/Zn^{2+} Storage, Adv. Mater. (2025) 2501624, https://doi.org/10.1002/adma.202501624.

[2] X. Hu, S. Gao, T. Lin, X. Peng, Y. Huang, Y. Zhang, X. Yang, L. Wang, G. Luo, Z. Wen, Iodine–Doped Sodium Vanadate Cathode for Improved Zn Ion Diffusion Kinetics, Adv. Mater. (2025) 2416714, https://doi.org/10.1002/adma.202416714.

[3] K.–S. Jhang, C.–Y. Tseng, H.–Y. Tuan, Cation Disorder–Driven d–Band Center Engineering and Dual–Mode Phonon Coupling Enable Ultrastable, High–Rate K^+ Storage in Ge–Sn Chalcogenides, Adv. Funct. Mater. (2025) e18968, https://doi.org/10.1002/adfm.202518968.

[4] Y.–Y. Tseng, H.–Y. Tuan, Coherent Single–Atom Dipole–Dipole Coupling Mediates Holistic Regulation of K^+ Migration for Superior Energy Storage and Dendrite–Free Metal Deposition, Adv. Funct. Mater. (2025) 2423387, https://doi.org/10.1002/adfm.202423387.

[5] K.–T. Chen, S. Chong, L. Yuan, Y.–C. Yang, H.–Y. Tuan, Conversion–alloying dual mechanism anode: Nitrogen–doped carbon–coated Bi_2Se_3 wrapped with graphene for superior potassium–ion storage, Energy Storage Mater. 39 (2021) 239–249, https://doi.org/10.1016/j.ensm.2021.04.019.

[6] H. Ni, Z. Fan, J. Wang, Y. Wu, Research Progress on the Mechanisms of MOF/COF and Their Derivatives in Zinc−Ion Batteries, Energy Storage Mater. (2025) 104220, https://doi.org/10.1016/j.ensm.2025.104220.

[7] Q. Zhang, S. Ju, S. Zhang, S. Xu, Z. Zhang, A Multi‐Colored, Structure−Tolerant Vanadate Cathode for High−Performance Aqueous Zinc−Ion Batteries, Adv. Energy Mater. 15(18) (2025) 2404597, https://doi.org/10.1002/aenm.202404597.

[8] T. Li, A. Naveed, J. Zheng, B. Chen, M. Jiang, B. Liu, Y. Zhou, X. Li, M. Su, R. Guo, Engineering aqueous electrolytes with vicinal S−based organic additives for

highly reversible zinc−ion batteries, Angew. Chem. Int. Ed. 2025, 64, e202424095, https://doi.org/10.1002/anie.202424095.

[9] D. Zhang, J. Cao, C. Yang, K. Lolupiman, W. Limphirat, X. Wu, X. Zhang, J. Qin, Y. Huang, Highly Stable Aqueous Zn‐Ion Batteries Achieved by Suppressing the Active Component Loss in Vanadium–Based Cathode, Adv. Energy Mater. 15(15) (2025) 2404026, https://doi.org/10.1002/aenm.202404026.

[10] D. Wang, C. Wen, T. Liu, Y. Wu, Y. Wei, J. Tu, G. Zhu, Z. Zhou, Z. Tu, Dual Regulation of Bulk Heterostructure and Engineered Cathode–Electrolyte Interphase in Vanadium Cathodes for Durable Zinc Storage, Adv. Funct. Mater. (2025) e18162, https://doi.org/10.1002/adfm.202518162.

[11] L. Mai, X. Tian, Y. Zhao, Air taxis will soon be in our skies—if batteries can be made safer, Nature. 645 (8079) (2025) 36–38, https://doi.org/10.1038/d41586–025–02758–6.

[12] H. Li, R. Jia, W. Chen, C. Wei, Q. Ji, X. Long, B. Wang, K. Zhang, J. Feng, L. Tan, Bio–Based Separator Engineering Toward Better Metal Anodes in Rechargeable Batteries: Progress and Perspectives, Adv. Funct. Mater. (2025) e12051, https://doi.org/10.1002/adfm.202512051.

[13] X. Gu, J. Wang, X. Zhao, X. Jin, Y. Jiang, P. Dai, N. Wang, Z. Bai, M. Zhang, M. Wu, Engineered nitrogen doping on VO_2 (B) enables fast and reversible zinc–ion storage capability for aqueous zinc–ion batteries, J. Energy Chem. 85 (2023) 30–38, https://doi.org/10.1016/j.jechem.2023.05.043.

[14] D. Gupta, S. Liu, R. Zhang, Z. Guo, Future Long Cycling Life Cathodes for Aqueous Zinc–Ion Batteries in Grid–Scale Energy Storage, Adv. Energy Mater. 15(18) (2025) 2500171, https://doi.org/10.1002/aenm.202500171.

[15] G. Yoo, Y.–G. Lee, B. Im, D.–G. Kim, Y.–R. Jo, Integrated solution for a stable and high–performance zinc–ion battery using an electrolyte additive, Energy Storage Mater. 61 (2023) 102845, https://doi.org/10.1016/j.ensm.2023.102845.

[16] S. Liu, Y. Liao, T. Liu, L. Chen, Q. Zhang, Electrochemical activation of vanadium–based cathodes in aqueous zinc–ion batteries: advances, challenges and prospects, Energy Storage Mater. 73 (2024) 103799, https://doi.org/10.1016/j.ensm.2024.103799.

[17] Y.–Y. Hsieh, H.–Y. Tuan, Emerging trends and prospects in aqueous electrolyte design: Elevating energy density and power density of multivalent metal–ion batteries, Energy Storage Mater. 68 (2024) 103361, https://doi.org/10.1016/j.ensm.2024.103361.

[18] P. Xu, M. Xu, J. Zhang, J. Zou, Y. Shi, D. Luo, D. Wang, H. Dou, Z. Chen, In–Situ Solid Electrolyte Interface via Dual Reaction Strategy for Highly Reversible Zinc Anode, Angew. Chem. Int. Ed. 63(41) (2024) e202407909, https://doi.org/10.1002/anie.202407909.

[19] L. Song, Q. Yang, Y. Yao, M. Tan, R. Li, J. Liao, X. Zhou, Y. Yu, Surface Work Function–Induced High–Entropy Solid Electrolyte Interphase Formation for Highly Stable Potassium Metal Anodes, Angew. Chem. Int. Ed. (2025) e202509252, https://doi.org/10.1002/anie.202509252.

[20] L. You, S. Guo, Y. He, Y. Xie, S. Liang, G. Fang, Surface Tension–Derived Electrical Double Layer Modification Enables Practical Zinc–Ion Pouch Cells, Adv. Funct. Mater. (2025) 2500780, https://doi.org/10.1002/adfm.202500780.

[21] Q. Xiao, S. He, P. Liu, M. Ge, Y. Li, Y. Zhu, Y. Lin, C. Wang, Q. Wang, Multifunctional Silanol‐Based Film–Forming Additive for Stable Zn Anode, Adv. Funct. Mater. 35(12) (2025) 2417708, https://doi.org/10.1002/adfm.202417708.

[22] J. Li, Y. Long, X. Yu, J. Li, N. Li, J. Han, J. Wang, Z. Yang, Polymeric acid additive strategy for long–lifetime aqueous zinc–ion batteries, Energy Storage Mater. 76 (2025) 104154, https://doi.org/10.1016/j.ensm.2025.104154.

[23] P. Xue, C. Guo, W. Gong, Y. Chen, X. Chen, X. Li, J. Yang, Q. Zhang, K. Davey, K. Zhu, Multifunctional Polymer Interphase with Fast Kinetics for Ultrahigh–rate Zn Metal Anode, Angew. Chem. Int. Ed. 64(16) (2025) e202500295, https://doi.org/10.1002/anie.202500295.

[24] D. Luo, X. Ma, P. Du, Z. Chen, Q. Lin, Y. Liu, B. Niu, X. He, X. Wang, Reconstructing Solvation Structure by Steric Hindrance–Coordination Push‐Pull of Dipolymer–H_2O–Zn^{2+} toward Long–life Aqueous Zinc–Metal Batteries, Angew. Chem. Int. Ed. 63(28) (2024) e202401163, https://doi.org/10.1002/anie.202401163.

[25] Y. Zhang, Y. Zhang, X. Wang, H. Gong, Y. Cao, K. Ma, S. Zhang, S. Wang, W. Yang, L. Wang, Trace Multifunctional Additive Enhancing 4.8 V Ultra–High Voltage Performance of Ni–Rich Cathode and SiO_x Anode Battery, Adv. Energy Mater. 15(5) (2025) 2403751, https://doi.org/10.1002/aenm.202403751.

[26] H. Li, Y. Li, M. Liu, Z. Yang, Y. Gong, J. Qian, R. Zhang, Y. Bai, F. Wu, C. Wu, Biocrust–inspired interface layer with dual functions towards highly reversible zinc metal anodes, Energy Environ. Sci. 18(6) (2025) 2973–2984, https://doi.org/10.1039/D4EE06048B.

[27] A. Ye, Z. Zhu, Z. Ji, X. He, Y. He, X. Fu, W. Yang, Y. Wang, Electrochemical Active Micro–Protein Coating by Self–Assembling 2D–Microfluidics for Stabilizing Lithium Metal Anode, Adv. Funct. Mater. 34(6) (2024) 2310593, https://doi.org/10.1002/adfm.202310593.

[28] Y. Kang, D. Lin, B. Liu, N. Dong, Z. Zhao, G. Tian, S. Qi, D. Wu, In Situ Engineering of a 3D Branched Polyimide/Silver Interface Layer with Dual Ion–

Electron Conductivity for Superior Structural Integrity and Long–Cycle Stability of Silicon Anodes, Adv. Funct. Mater. (2025) 2504861, https://doi.org/10.1002/adfm.202504861.

[29] X. Xiao, L. Zhang, W. Xin, M. Yang, Y. Geng, M. Niu, H. Zhang, Z. Zhu, Self–Assembled Layer of Organic Phosphonic Acid Enables Highly Stable MnO_2 Cathode for Aqueous Znic Batteries, Small. 20(24) (2024) 2309271, https://doi.org/10.1002/smll.202309271.

[30] P. Ma, Z. Zhang, J. Wang, H. Li, H.–Y. Yang, Y. Shi, Self–assembled 2D $VS_2/Ti_3C_2T_x$ MXene nanostructures with ultrafast kinetics for superior electrochemical sodium–ion storage, Adv. Sci. 10(31) (2023) 2304465, https://doi.org/10.1002/advs.202304465.

[31] L. Xu, S. Xue, X. Jia, R. Liu, L. Wang, L. Tao, J. Yao, J. Zhang, H. Wan, Y. Wang, Branch Chain Variations Modulate Pyridine Derivative Adsorption for Long–Life Zinc–Ion Battery, Adv. Funct. Mater. (2025) 2425372, https://doi.org/10.1002/adfm.202425372.

[32] Y. Zhang, Q. Li, W. Feng, H. Yue, S. Gao, Y. Su, Y. Tang, J. Wu, Z. Zhang, Y. Zhang, Valence engineering via polyoxometalate‐induced on vanadium centers for efficient aqueous zinc–ion batteries, Angew. Chem. Int. Ed. 137(19) (2025) e202501728, https://doi.org/10.1002/anie.202501728.

[33] X. Lu, L. Chen, W. Li, X. Zhang, W. Chi, S. Li, C. Wang, Y. Liu, X. Zhang, Cation‐Anion Coordination for Covalent Anchoring of Manganese Oxides to Stabilize Mn Ion Valence and Suppress Jahn–Teller Distortion and Dissolution, Energy Environ. Mater. e70061, https://doi.org/10.1002/eem2.70061.

[34] W. Kou, Z. Fang, H. Ding, W. Luo, C. Liu, L. Peng, X. Guo, W. Ding, W. Hou, Valence Engineering Boosts Kinetics and Storage Capacity of Layered Double

Hydroxides for Aqueous Magnesium–Ion Batteries, Adv. Funct. Mater. 34(41) (2024) 2406423, https://doi.org/10.1002/adfm.202406423.

[35] J. Zhang, H. Yuan, Z. Qin, P. Ding, D. Yu, H. Wu, J. Wang, Y. Shao, W. Zhou, C.–W. Nan, Regulating the Manganese Valence State Improves the Kinetic Properties of Manganese–Based Cathodes, Adv. Funct. Mater. 35(3) (2025) 2413684, https://doi.org/10.1002/adfm.202413684.

[36] W. Deng, C. Li, W. Zou, Y. Xu, Y. Chen, R. Li, Understanding the Super–Theoretical Capacity Behavior of VO_2 in Aqueous Zn Batteries, Small. 20(19) (2024) 2309527, https://doi.org/10.1002/smll.202309527.

[37] S. Li, G. Zhang, Q. Li, T. He, X. Sun, A facile self-saturation process enabling the stable cycling of a small molecule menaquinone cathode in aqueous zinc batteries, Chemical Science 15(43) (2024) 17971-17978, https://doi.org/10.1039/D4SC04685D.

[38] Z. Wang, P. Cui, X. Wang, M. Chang, Y. Yu, J. You, F. Hu, Y. Wu, K. Zhu, Co–substitution engineering boosting the kinetics and stablity of VO_2 for Zn ion batteries, Adv. Funct. Mater. 34(46) (2024) 2407925, https://doi.org/10.1002/adfm.202407925.

[39] Z. Zhang, B. Xi, X. Wang, X. Ma, W. Chen, J. Feng, S. Xiong, Oxygen defects engineering of $VO_2 \cdot xH_2O$ nanosheets via in situ polypyrrole polymerization for efficient aqueous zinc ion storage, Adv. Funct. Mater. 31(34) (2021) 2103070, https://doi.org/10.1002/adfm.202103070.

[40] H.–Y. Tuan, A. Ghezelbash, B.A. Korgel, Silicon nanowires and silica nanotubes seeded by copper nanoparticles in an organic solvent, Chem. Mater. 20(6) (2008) 2306–2313, https://doi.org/10.1021/cm703304r.

[41] C. Zhang, Z.–H. Wu, C.–Q. Yang, X.–Z. Guo, Y.–X. Yu, Y. Yang, Rational regulation of optimal oxygen vacancy concentrations on VO_2 for superior aqueous

zinc–ion battery cathodes, ACS Appl. Mater. Interfaces. 16(31) (2024) 40903–40913, https://doi.org/10.1021/acsami.4c05618.

[42] J.–J. Ye, P.–H. Li, H.–R. Zhang, Z.–Y. Song, T. Fan, W. Zhang, J. Tian, T. Huang, Y. Qian, Z. Hou, Manipulating oxygen vacancies to spur ion kinetics in V_2O_5 structures for superior aqueous zinc–ion batteries, Adv. Funct. Mater. 33(46) (2023) 2305659, https://doi.org/10.1002/adfm.202305659.

[43] J. Guo, B. He, W. Gong, S. Xu, P. Xue, C. Li, Y. Sun, C. Wang, L. Wei, Q. Zhang, Emerging amorphous to crystalline conversion chemistry in Ca–doped VO_2 cathodes for high–capacity and long–term wearable aqueous zinc–ion batteries, Adv. Mater. 36(11) (2024) 2303906, https://doi.org/10.1002/adma.202303906.

[44] T. Wang, W. Zhao, Y. Miao, A. Cui, C. Gao, C. Wang, L. Yuan, Z. Tian, A. Meng, Z. Li, Enhancing defect–induced dipole polarization strategy of SiC@ MoO_3 nanocomposite towards electromagnetic wave absorption, Nano–Micro Lett. 16(1) (2024) 273, https://doi.org/10.1007/s40820–024–01478–2.

[45] T. Xue, Y. Mu, Z. Zhang, J. Guan, J. Qiu, C. Yang, L. Zang, L. Zeng, Enhanced Zinc Deposition and Dendrite Suppression in Aqueous Zinc–Ion Batteries Via Citric Acid–Aspartame Electrolyte Additives, Adv. Energy Mater. (2025) 2500674, https://doi.org/10.1002/aenm.202500674.

[46] J. Kang, S. Lee, H. Lee, Dual Electrolyte Additives Suppress Hydrogen Evolution in Aqueous Li–Ion Batteries, ACS Energy Lett. 10(6) (2025) 2593–2599, https://doi.org/10.1021/acsenergylett.5c00800.

[47] Y. Huang, H. Yan, W. Liu, F. Kang, Transforming Zinc‐Ion Batteries with DTPA–Na: A Synergistic SEI and CEI Engineering Approach for Exceptional Cycling Stability and Self–Discharge Inhibition, Angew. Chem. Int. Ed. 136(48) (2024) e202409642, https://doi.org/10.1002/ange.202409642.

[48] H. Yu, Y. Cao, L. Chen, Y. Hu, X. Duan, S. Dai, C. Li, H. Jiang, Surface enrichment and diffusion enabling gradient–doping and coating of Ni–rich cathode toward Li–ion batteries, Nat. Commun. 12(1) (2021) 4564, https://doi.org/10.1038/s41467–021–24893–0.

[49] Z. Wang, P. Zhang, J. Zhang, K. Tang, J. Cao, Z. Yang, S. Qin, J.M. Razal, W. Lei, D. Liu, Dendrite–free zinc deposition enabled by MXene/nylon scaffold and polydopamine solid–electrolyte interphase for flexible zinc–ion batteries, Energy Storage Mater. 67 (2024) 103298, https://doi.org/10.1016/j.ensm.2024.103298.

[50] T.-H. Wu, J.-H. Su, Y.-C. Lin, Capacity-stability trade-off phenomenon: voltage-tuned electrochemical activation of vanadium oxides in aqueous zinc-ion batteries, Journal of Power Sources 661 (2026) 238683, https://doi.org/10.1016/j.jpowsour.2025.238683.

[51] S.–H. Lee, H.–M. Cheong, M.–J. Seong, P. Liu, C.–E. Tracy, A. Mascarenhas, J.R. Pitts, S.–K. Deb, Raman spectroscopic studies of amorphous vanadium oxide thin films, Solid State Ion. 165(1–4) (2003) 111–116, https://doi.org/10.1016/j.ssi.2003.08.022.

[52] R. Roy, P. Sharma, G. Mahendra, P. Dutta, V. Raghuraman, P. Singh, A.K. Singh, Thermo‐Electrochemical Tuning of V_2O_5 to ZnV_3O_8 Enables Ultra–Stable Zinc–Ion Battery, Adv. Energy Mater. e02262, https://doi.org/10.1002/aenm.202502262.

[53] K. Zhu, T. Wu, K. Huang, A high-voltage activated high-erformance cathode for aqueous Zn-ion batteries, Energy Storage Materials 38 (2021) 473-481, https://doi.org/10.1016/j.ensm.2021.03.031.

[54] H. Luo, B. Wang, F. Wang, J. Yang, F. Wu, Y. Ning, Y. Zhou, D. Wang, H. Liu, S. Dou, Anodic oxidation strategy toward structure-optimized V2O3 cathode via

electrolyte regulation for Zn-ion storage, Acs Nano 14(6) (2020) 7328-7337, https://doi.org/10.1021/acsnano.0c02658.

[55] Y. Wang, J. Zhu, H. Liang, W. Zhai, J. Li, J. Wu, H. Chu, H. Wei, Enhanced zinc-ion storage performance in cerium-modified layered vanadium oxides with stable oxygen vacancies, Chemical Engineering Journal (2025) 163515, https://doi.org/10.1016/j.cej.2025.163515.

[56] B. Yang, K. Li, C. Yang, Y. Zhang, Y. Gong, Orbital hybridization and electron transfer triggered by V–dopant and symmetry breakage to stabilize low–valent Mn for zinc–ion batteries, Chem. Eng. J. (2025) 163032, https://doi.org/10.1016/j.cej.2025.163032.

[57] L. Tan, Z. Li, L. Wang, Y. Shang, Z. Wang, Z. Tong, Y. Li, X. Li, Enhancing ion shuttling through hydrogen bonding effect in ZnV_2O_4 aqueous zinc ion battery cathode, Chem. Eng. J. (2025) 162143, https://doi.org/10.1016/j.cej.2025.162143.

[58] K. Guo, Z. Song, Y. Lv, L. Gan, M. Liu, Inorganic–Organic Co–Intercalated $[Al_{0.16}(C_5H_{14}ON)_{0.12}]V_2O_5 \cdot 0.39\ H_2O$ Cathode for High–Performance Aqueous Zinc–Ion Batteries, Adv. Funct. Mater. (2025) 2506036, https://doi.org/10.1002/adfm.202506036.

[59] Z.–H. Wu, Z.–Q. Yang, Y.–X. Yu, In situ synthesis of VO_2 containing high–valent vanadium via surface oxidation of V_2C MXene for robust near–interface reactions in aqueous zinc–ion batteries, Chem. Eng. J. 511 (2025) 162146, https://doi.org/10.1016/j.cej.2025.162146.

[60] L. Pan, Y. Sun, S. Yao, Y. Zhang, Z. Wen, Stable structure and oxygen–rich vacancy assist $NH_4V_4O_{10}$ to become a high–performance aqueous zinc–ion battery cathode material, J. Alloys Compd. 1010 (2025) 177949, https://doi.org/10.1016/j.jallcom.2024.177949.

[61] S. Yao, Y. Sun, L. Pan, Pre–removing partial ammonium ion induces vanadium vacancy assist $NH_4V_4O_{10}$ as a high–performance aqueous zinc ion battery cathode, Appl. Surf. Sci. 672 (2024) 160785, https://doi.org/10.1016/j.apsusc.2024.160785.

[62] K. Lolupiman, C. Yang, P. Woottapanit, W. Sukmas, W. Limphirat, N. Rodthongkum, X. Zhang, G. He, J. Qin, Sulfur - Doped Vanadium Oxide for High - Performance and Stable Cathode Material of Zinc - Ion Batteries, Advanced Functional Materials (2025) e24100, https://doi.org/10.1002/adfm.202524100.

[63] K. LOLUPIMA, J. Cao, D. ZHANG, C. YANG, X. ZHANG, J. QIN, A review on the development of metals-doped Vanadium oxides for zinc-ion battery, Journal of Metals, Materials and Minerals 34(3) (2024) 2084-2084, https://doi.org/10.55713/jmmm.v34i3.2084.

[64] D. Zhang, Y. Yue, C. Yang, W. Limphirat, X. Zhang, J. Qin, J. Cao, Kinetics-Boosted and Dissolution-Suppressed Molybdenum-Doped vanadium dioxide for Long-Life Zinc-Ion batteries, Chemical Engineering Journal 506 (2025) 160160, https://doi.org/10.1016/j.cej.2025.160160.

[65] Z. Dai, C. Yang, J. Cao, X. Zhang, Y. Zhao, D. Zhang, X. Zhang, J. Qin, Cathode-electrolyte interface modification by electrolyte engineering for vanadium-based zinc-ion batteries, Chemical Engineering Journal (2025) 164027, https://doi.org/10.1016/j.cej.2025.164027.

[66] Q. He, T. Hu, Q. Wu, C. Wang, X. Han, Z. Chen, Y. Zhu, J. Chen, Y. Zhang, L. Shi, Tunnel–Oriented VO_2 (B) Cathode for High–Rate Aqueous Zinc–Ion Batteries, Adv. Mater. 36(25) (2024) 2400888, https://doi.org/10.1002/adma.202400888.

[67] C.–B. Chang, Y.–Y. Tseng, Y.–R. Lu, Y.–C. Yang, H.–Y. Tuan, High Entropy Induced Local Charge Enhancement Promotes Frank–Van der Merwe Growth for

Dendrite–Free Potassium Metal Batteries, Adv. Funct. Mater. 34(52) (2024) 2411193, https://doi.org/10.1002/adfm.202411193.

[68] C.–Y. Tsai, C.–H. Chang, T.–L. Kao, K.–T. Chen, H.–Y. Tuan, Shape matters: $SnP_{0.94}$ teardrop nanorods with boosted performance for potassium ion storage, Chem. Eng. J. 417 (2021) 128552, https://doi.org/10.1016/j.cej.2021.128552.

[69] Y.–Y. Hsieh, H.–Y. Tuan, Architectural van der Waals Bi_2S_3/Bi_2Se_3 topological heterostructure as a superior potassium–ion storage material, Energy Storage Mater. 51 (2022) 789–805, https://doi.org/10.1016/j.ensm.2022.07.020.

[70] Z. Peng, S. Li, L. Tang, J. Zheng, L. Tan, Y. Chen, Water–shielding electric double layer and stable interphase engineering for durable aqueous zinc–ion batteries, Nat. Commun. 16(1) (2025) 4490, https://doi.org/10.1038/s41467–025–59830–y.

[71] M. Yang, M. Chuai, M. Lai, J. Zhu, Y. Wang, Q. Hu, M. Chen, J. Chen, K. Fang, G. Chai, Customizable crystalline–amorphous rectifying heterostructure cathodes for durable and super–fast zinc storage, Energy Environ. Sci. 18(10) (2025) 4651–4664, https://doi.org/10.1039/D5EE00304K.

[72] Y.–Y. Hsieh, Y.–C. Chuang, H.–Y. Tuan, Unraveling Dual Mechanisms in Quasi–Layered Bi_2O_2Se via Defect Modulation for High–Performance Aqueous Zn–Ion Batteries, Adv. Funct. Mater. 34(46) (2024) 2406975, https://doi.org/10.1002/adfm.202406975.

[73] C.–W. Chou, H.–Y. Tuan, Whispers of Entropic Distortion Elevating Voltage and Electrochemical Depth in Potassium Hexacyanoferrate Cathodes, Adv. Funct. Mater. 35(14) (2025) 2418680, https://doi.org/10.1002/adfm.202418680.

[74] C.–H. Chang, K.–T. Chen, Y.–Y. Hsieh, C.–B. Chang, H.–Y. Tuan, Crystal facet and architecture engineering of metal oxide nanonetwork anodes for high–

performance potassium ion batteries and hybrid capacitors, ACS nano. 16(1) (2022) 1486–1501, https://doi.org/10.1021/acsnano.1c09863.

[75] S. Chen, F. Yu, H. Deng, W. Chen, H. Sun, J. Zhu, B. Lu, Selective Catalysis–Mediated Interface to Stabilize Antimony Atom–Cluster Anode for Robust Potassium–Ion Batteries, Angew. Chem. Int. Ed. 2025, e202511870, https://doi.org/10.1002/anie.202511870.

[76] B. Liu, X. Ma, Q. Wang, S. Zhang, J. Yuwono, H. Jin, J. Qiu, H. Ma, C. Wang, C. Lai, Designing copolymeric SEI layer based on click reaction toward ultralow N/P ratio and long cycle life zinc ion batteries, Adv. Energy Mater. 15(16) (2025) 2404660, https://doi.org/10.1002/aenm.202404660.

[77] D. Li, C. Li, W. Liu, H. Bu, X. Zhang, T. Li, J. Zhang, M. Kong, X. Wang, C. Wang, Constructing a multifunctional SEI layer enhancing kinetics and stabilizing zinc metal anode, Adv. Funct. Mater. 35(6) (2025) 2415107, https://doi.org/10.1002/adfm.202415107.

[78] Y. Bai, Y. Qin, J. Hao, H. Zhang, C.M. Li, Advances and perspectives of ion–intercalated vanadium oxide cathodes for high‐performance aqueous zinc ion battery, Adv. Funct. Mater. 34(11) (2024) 2310393, https://doi.org/10.1002/adfm.202310393.

[79] L. Xing, X. Zhang, N. Xu, P. Hu, K. Wang, Q. An, Mechanistic Insights of Zn–Ion Storage in Synergistic Vanadium–Based Composites, Adv. Funct. Mater. 34(14) (2024) 2312773, https://doi.org/10.1002/adfm.202312773.

[80] S. Guo, M. Yao, S. Liang, G. Fang, Failure Mechanisms and Practical Optimizations for Ah–Scale Aqueous Zinc–Ion Pouch Cells, Adv. Mater. (2025) e12364, https://doi.org/10.1002/adma.202512364.

[81] J. Zhai, W. Zhao, L. Wang, J. Shuai, R. Chen, W. Ge, Y. Zong, G. He, X. Wang, Ultrathin cellulosic gel electrolytes with a gradient hydropenic interface for stable,

high–energy and flexible zinc batteries, Energy Environ. Sci. 18(9) (2025) 4241–4250, https://doi.org/10.1039/D5EE00158G.

[82] X. Ding, Q. Zhu, Y. Fan, Y. Yang, L. Liu, Y. Shao, Y. Xiao, C.–H. Wu, L. Han, High–entropy V–based cathode for high–capacity and long–life aqueous zinc–ion battery, Nano Energy. 136 (2025) 110701, https://doi.org/10.1016/j.nanoen.2025.110701.

[83] Y. Liu, C. Gao, Y. Sun, X. Hao, Z. Pi, M. Yang, X. Zhao, K. Cai, Enhancing the electrochemical activation kinetics of V_2O_3 for high–performance aqueous zinc–ion battery cathode materials, Chem. Eng. J. 490 (2024) 151535, https://doi.org/10.1016/j.cej.2024.151535.

[84] D. Wang, C. Wen, G. Zhu, J. Tu, K. Kang, Y. Qi, B. Zhang, Z. Zhou, Modifying V_2O_5 structure with bio–additive via thermal reconfiguration for enhanced cathode in aqueous zinc ion batteries, Chem. Eng. J. 512 (2025) 162448, https://doi.org/10.1016/j.cej.2025.162448.

[85] D. Chen, M. Yang, Y. Ming, W. Cai, S. Shi, Y. Pan, X. Hu, R. Yu, Z. Wang, B. Fei, Synergetic Effect of Mo‐Doped and Oxygen Vacancies Endows Vanadium Oxide with High–Rate and Long–Life for Aqueous Zinc Ion Battery, Small. 20(48) (2024) 2405168, https://doi.org/10.1002/smll.202405168.

Declaration of Competing Interest

■ The authors declare that they have no known competing financial interests or personal relationships that could have appeared to influence the work reported in this paper.

□ The authors declare the following financial interests/personal relationships which may be considered as potential competing interests:

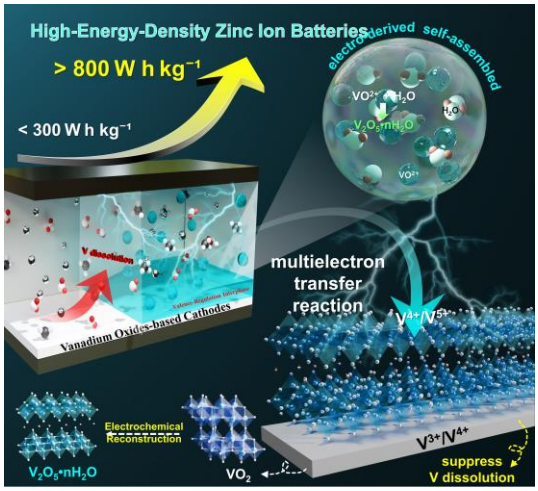

An electro-driven strategy regulates interphase self-assembly and in situ reconstruction in VO_2 cathodes. Current induces the formation of dense V^{5+}-rich interphases while simultaneously reconstructing the bulk into hydrated $V_2O_5 \cdot nH_2O$. These synergistic processes homogenize Zn^{2+} flux, inhibit vanadium dissolution, and expose abundant electroactive sites, delivering exceptional energy and power densities for aqueous zinc-ion batteries.

Hightlights

- An electro-driven self-assembly strategy constructs adaptive and valence-regulating interphases on VO_2 cathodes.
- Tuning activation kinetics (0.5 A g^{-1} vs 0.1 A g^{-1}) enables precise control of interphase uniformity and stability.
- The dense interphase promotes homogeneous electric fields, suppresses vanadium dissolution, and enhances Zn^{2+} transport.
- In situ $VO_2 \rightarrow V_2O_5 \cdot nH_2O$ reconstruction enables reversible multielectron V^{4+}/V^{5+} transitions and fast redox kinetics.
- Pouch cells deliver 842.8 W h kg^{-1} and 14,769.5 W kg^{-1}, ranking among the highest reported for AZIBs.